A Fully Automatic Approach for Multimodal PET and MR Image Segmentation in Gamma Knife Treatment Planning

Leonardo Rundo[1,2], Alessandro Stefano[1,3], Carmelo Militello[1], Giorgio Russo[1,4], Maria Gabriella Sabini[4], Corrado D'Arrigo[4], Francesco Marletta[4], Massimo Ippolito[4], Giancarlo Mauri[2], Salvatore Vitabile[5], Maria Carla Gilardi[1]

[1] Istituto di Bioimmagini e Fisiologia Molecolare - Consiglio Nazionale delle Ricerche (IBFM-CNR), Cefalù (PA), Italy

[2] Dipartimento di Informatica, Sistemistica e Comunicazione (DISCo), Università degli Studi di Milano-Bicocca, Milano, Italy

[3] Dipartimento di Ingegneria Chimica, Gestionale, Informatica, Meccanica (DICGIM), Università degli Studi di Palermo, Palermo, Italy

[4] Azienda Ospedaliera per l'Emergenza Cannizzaro, Catania, Italy

[5] Dipartimento di Biopatologia e Biotecnologie Mediche (DIBIMED), Università degli Studi di Palermo, Palermo, Italy

Abstract

Background and Objectives: Nowadays, clinical practice in Gamma Knife treatments is generally based on MRI anatomical information alone. However, the joint use of MRI and PET images can be useful for considering both anatomical and metabolic information about the lesion to be treated. In this paper we present a co-segmentation method to integrate the segmented Biological Target Volume (BTV), using [^{11}C]-Methionine-PET (MET-PET) images, and the segmented Gross Target Volume (GTV), on the respective co-registered MR images. The resulting volume gives enhanced brain tumor information to be used in stereotactic neuro-radiosurgery treatment planning.

GTV often does not match entirely with BTV, which provides metabolic information about brain lesions. For this reason, PET imaging is valuable and it could be used to provide complementary information useful for treatment planning. In this way, BTV can be used to modify GTV, enhancing Clinical Target Volume (CTV) delineation.

Methods: A novel fully automatic multimodal PET/MRI segmentation method for Leksell Gamma Knife® treatments is proposed. This approach improves and combines two computer-assisted and operator-independent single modality methods, previously developed and validated, to segment BTV and GTV from PET and MR images, respectively. In addition, the GTV is

utilized to combine the superior contrast of PET images with the higher spatial resolution of MRI, obtaining a new BTV, called BTV_{MRI}.

A total of 19 brain metastatic tumors, undergone stereotactic neuro-radiosurgery, were retrospectively analyzed. A framework for the evaluation of multimodal PET/MRI segmentation is also presented. Overlap-based and spatial distance-based metrics were considered to quantify similarity concerning PET and MRI segmentation approaches. Statistics was also included to measure correlation among the different segmentation processes. Since it is not possible to define a gold-standard CTV according to both MRI and PET images without treatment response assessment, the feasibility and the clinical value of BTV integration in Gamma Knife treatment planning were considered. Therefore, a qualitative evaluation was carried out by three experienced clinicians.

Results: The achieved experimental results showed that GTV and BTV segmentations are statistically correlated (Spearman's rank correlation coefficient: 0.898) but they have low similarity degree (average Dice Similarity Coefficient: 61.87 ± 14.64). Therefore, volume measurements as well as evaluation metrics values demonstrated that MRI and PET convey different but complementary imaging information. GTV and BTV could be combined to enhance treatment planning. In more than 50% of cases the CTV was strongly or moderately conditioned by metabolic imaging. Especially, BTV_{MRI} enhanced the CTV more accurately than BTV in 25% of cases.

Conclusions: The proposed fully automatic multimodal PET/MRI segmentation method is a valid operator-independent methodology helping the clinicians to define a CTV that includes both metabolic and morphologic information. BTV_{MRI} and GTV should be considered for a comprehensive treatment planning.

1.   Introduction

Leksell Gamma Knife® (Elekta, Stockholm, Sweden) is a stereotactic radiosurgical device to treat different brain disorders that are often inaccessible for conventional surgery, such as benign or malignant tumors, arteriovenous malformations and trigeminal neuralgia [1][2]. Stereotactic radiosurgery allows an accurate external irradiation (with a single, high dose and steep dose gradient) to minimize doses given to adjacent critical brain structures. The gamma rays (generated by Cobalt-60 [^{60}Co] radioactive sources) are focused on the target through a metal helmet. A personalized treatment plan is implemented using the Leksell Gamma Plan® treatment planning system. Currently, the Gamma Plan software does not support DICOM-RT objects (generated for the radiation therapy workflow [3] and does not allow to import/export any external ROIs (neither manually nor automatically calculated). In addition, the Gamma Plan software does not provide automatic image processing methods.

Nowadays, *Gross Tumor Volume (GTV)* is usually delineated on anatomical Magnetic Resonance Imaging (MRI) alone, acquired a few hours before treatment, by means of a fully manual process. Manual segmentation has two main drawbacks: (i) time-expensiveness, because dozens of slices have to be manually segmented in a short time; (ii) operator-dependence in target volume definition. The repeatability of the tumor volume delineation may be ensured only by using computer-assisted methods, to support the treatment planning phase. Automated or semi-automated approaches can be of great help, providing higher intra- and inter-operator reliability compared to conventional manual tracing [4]. Consequently, stereotactic neuro-radiosurgery treatment effectiveness can be optimized using automatic methods to support clinicians in the planning phase and to improve treatment response assessment.

MRI is an important modality in radiation therapy planning and patient follow-up, complementing the use of Computed Tomography (CT) in target delineation. MRI provides several advantages over CT, including high quality detailed images and excellent soft-tissue

3

contrast, especially concerning the extent of brain cancer disease [5][6][7]. On the other hand, CT attenuation maps, used in radiotherapy for dose planning, are not available in MRI and geometric distortion could be manifested due to the static magnetic field non-uniformities [8]. However, stereotactic dose calculation algorithms utilize a simplified isocentric technique with a known beam profile and a constant linear attenuation through tissue [9], not performing dose painting for non-uniform radiation dose distribution. Gamma Plan system also assumes that the brain is composed entirely of unit density material [10] and dose delivery is based on the unit "shot" (i.e. a dose distribution approximately with spherical shape). Multiple shots are used in Gamma Knife treatment to deliver a conformal dose to an irregular radiosurgical target [11].

MRI is also considered to be superior to CT in determining the extent of tumor infiltration, although some histological evidence of malignancy may extend beyond the margin of enhancement [4]. In fact, typical MRI protocols, used for stereotactic radiosurgery treatment planning, include T1-weighted pre- and post-contrast (Gadolinium-enhanced) image of the head volume. Because of the infiltrative nature of glial and metastatic tumors, accurate delineation is difficult and the possibility for accurate determination of the appropriate target volume for treatment is limited. Moreover, in patients who underwent surgery, CT and MR imaging may not define tumor recurrence accurately. The integration of metabolic Positron Emission Tomography (PET) imaging may add another layer of sophistication to the use of radiosurgery in the treatment of gliomas and metastases. In addition, metabolic changes are often faster and more indicative of the effects caused by the therapy with respect to anatomical imaging [12]. Levivier *et al.* [13] used PET functional imaging in stereotactic conditions for the management of brain tumors, and found that it conveys independent metabolic information that is complementary to the anatomical information derived from CT or MR imaging.

In this regard, [^{11}C]-Methionine (MET) seems to have a potential role in providing additional information, although MRI remains the gold-standard for diagnosis and follow-up after radiation therapy [14][15]. Methionine is a natural amino acid avidly taken up by brain cancer

cells, whereas its uptake by normal cells is low. As a matter of fact, MET uptake is mainly from the activation of the L-mediated and A-mediated amino acid transport at the level of the Blood Brain Barrier (BBB) [16]. In this way, MET-PET discerns malign and benign tissues in brain tumors with great sensitivity and specificity, by localizing selectively in cancer regions of the brain. Numerous studies have shown that the specificity of the MET-PET for marking tumor delineation and for the differentiation relapse versus radiation necrosis is higher compared with MRI. In [17], metabolic imaging was used for biological target delineation in 36 patients that showed a significantly longer median survival compared with the group of patients in which target volume was merely defined by MRI.

In contrast, [18F]-Fluorodeoxyglucose (FDG) PET for metabolic target delineation, which was systematically analyzed by Gross *et al.* [18], showed limited clinical value when comparing brain tumor volume defined by PET with the corresponding volume defined by PET/MRI fusion images. Only in few patients, additional information was derived from FDG-PET for radiation treatment planning because of the low contrast between viable tumor and normal brain tissue, although FDG uptake is regionally related to anaplastic areas. The distribution of FDG, a glucose metabolism tracer, is thus not limited to malignant tissue because FDG enters the cells according to glucose transport mechanism [19].

The higher diagnostic accuracy of MET-PET is the rationale for using this diagnostic technique in target volume delineation of brain tumors: T1-weighted MRI alone cannot differentiate between treatment-related changes and residual tumor after neurosurgery, chemotherapy or radiation therapy [20]. Although the high contrast between tumor and normal tissue on PET images can reduce the inter- and intra-observer variability in tumor localization, the variability in tumor delineation with the qualitative use of PET is still high and often inconsistent with anatomically defined GTV [21]. Due to the nature of PET images (low spatial resolution and weak region boundaries), the *Biological Target Volume (BTV)* varies substantially depending on

the algorithm used to segment functional lesions: the choice of a standard method for PET volume contouring is a very challenging yet unresolved step [22].

Anatomical GTV often does not match with metabolic BTV at all. For this reason, MET-PET metabolic imaging is valuable and it could be used to provide additional information useful for treatment planning and enhanced tumor characterization [23]: the BTV can be used to modify the GTV in order to treat the actual cancer region more precisely. To improve the determination of lesion margin, it is necessary to combine the complementary information of tissues from both anatomical and functional imaging. Therefore, a reproducible multimodal PET/MRI segmentation method, which contextually segments tumors in each image domain, is mandatory. This task, named joint segmentation or co-segmentation, is a challenging problem due to: (i) unique demands and peculiarities brought by each imaging modality, and (ii) a lack of one-to-one region and boundary correspondences of lesions in different imaging modalities [24].

The implementation of molecular imaging, such as PET, into Gamma Knife treatment allows to better understand the biological activity about the cancer imaged on MRI. Especially for the brain tumors gaining deep insights about the cancer region is not always easy investigating MRI alone and it is needed to compare and, often, combine the information acquired by different imaging modalities. Applying contextually PET and MRI in Gamma Knife clinical scenarios showed that sometimes the BTV can contain metabolically active regions outside the GTV. In this case, combining both PET and MR imaging modalities is very important to improve the clinical outcome. Moreover, PET imaging requires computer-assisted segmentation methods to obtain an accurate BTV, minimizing operator-dependence and increasing result repeatability. As a matter of fact, this work is prominent for effective brain lesion therapy.

The proposed study investigates the impact of BTV segmentation, using MET-PET imaging, and the subsequent co-registration with MR images, utilized to delineate the GTV, in stereotactic neuro-radiosurgery therapy. A novel fully automatic multimodal segmentation

method for Leksell Gamma Knife treatment planning is proposed. Our previously developed PET [22][25][26] and MRI [27][28] segmentation methods have been exploited, improved, and properly combined together. The former uses the graph-based *Random Walker (RW)* algorithm [29] and the latter is based on unsupervised *Fuzzy C-Means (FCM)* clustering [30]. Both segmentation methods are valid operator-independent approaches to identify the BTV and the GTV, respectively, in order to delineate a comprehensive *Clinical Target Volume (CTV)* that includes metabolic and morphologic information, useful for treatment planning and patient follow-up. First of all, the Interesting Uptake Region (IUR), obtained on co-registered PET images using the graph-based BTV segmentation method, is exploited for the automatic generation of a suitable region including the tumor on MR brain images. These bounding regions, computed adaptively on MR images using a Level Set method, are then utilized by the GTV segmentation method. Lastly, GTV masks are combined with PET images to influence the BTV segmentation.

The presented multimodal segmentation approach yields the tumor boundaries in both PET and MRI modalities, conveying different information, which are not always complementary, considering that enhancement, edema, and necrosis regions are imaged differently by the modalities; so the tumor volumes defined on PET and on CT or MRI could be highly different [31].

The main key novelties of the proposed multimodal segmentation approach are:

- presenting a fully automatic method for GTV segmentation, calculated automatically by exploiting the IURs detected on PET images to define a suitable bounding region for the tumor zone with a Distance Regularized Level Set Evolution (DRLSE) approach;

- computing the BTV_{MRI}, which can reduce radioactivity spill-in and spill-out effects, between tumor and surrounding tissues, affecting the segmented BTV (according to the morphologic GTV information) and the subsequent BTV_{MRI} integration for a comprehensive treatment planning.

7

Co-segmentation tests on 19 metastatic brain tumors, treated with Leksell Gamma Knife radiosurgery, were retrospectively performed in order to evaluate the effectiveness of the proposed approach. Overlap-based and spatial distance-based metrics were calculated between PET and MRI segmentation results. Statistics was also considered to quantify correlation. Finally, a qualitative evaluation, based on a Likert score scale, was carried out by three experienced clinicians.

The manuscript is organized as follows: section 2 reports the state of the art on PET/CT and PET/MRI multimodal co-segmentation approaches; section 3 describes the MRI and MET-PET data as well as the proposed automatic multimodal PET/MRI segmentation method, its processing pipeline, and the used evaluation metrics for multimodal imaging; section 4 reports the experimental results and findings obtained in the segmentation tests; lastly, some discussions and conclusions are provided in sections 5 and 6, respectively.

2. Background

A huge number of monomodal segmentation methods on single image modalities (i.e. CT, MRI or PET) are present in the literature. Just a few studies address the segmentation of multimodal imaging data. In particular, we are interested in approaches that combine the complementary functional information conveyed by PET with the corresponding anatomical image scans (CT or MRI). In fact, in clinical use, it is highly desirable to have both functional and structural quantifiable information in a single scan so the disease can be both identified and localized, potentially resulting in an earlier diagnosis and more effective treatment plan.

In parallel to the developments of multimodal scanners (PET/CT and PET/MRI), there have been recent literature works trying to bring the usefulness of integrating anatomical and functional information into a common place for separating tumor tissues from normal structures. A concise but complete review of the state of the art regarding multimodal co-segmentation approaches is reported in the following, wherein each research paper is briefly explained.

8

Several studies deal with PET/CT tumor identification and characterization in radiation therapy scenarios. In [32], co-registered FDG-PET/CT images were used for the textural characterization of head and neck cancer (HNC) in radiotherapy treatment planning. After a manual segmentation on co-registered PET/CT images (performed by an experienced radiation oncologist), useful textural features were selected for distinguishing tumor from normal tissue in HNC subjects. Both k-nearest neighbors (KNNs) and decision tree (DT)-based KNN classifiers were employed to discriminate images of cancerous and healthy tissues. Han *et al.* [21] presented a Markov random field (MRF)-based co-segmentation of the PET/CT image pair with a regularized term that penalizes the segmentation difference between PET and CT. This graph-based method utilizes the strength of PET and CT modalities for target delineation in a group of 16 patients with HNC. Background and foreground seed voxels must be always manually identified by the user. A similar approach is reported in [31], where the segmentation is seen as a minimization problem of a MRF model, which encodes the information from both modalities. This optimization is solved using a graph-cut based method, by constructing two sub-graphs for PET and CT segmentation, respectively, and adding inter-subgraph arcs. The overall approach is semi-automatic, because initial seed points are required for the graph-based co-segmentation: one center point and two radii are given by the user. The algorithm was validated in robust delineation of lung tumors on 23 PET/CT datasets and two HNC subjects. A further MRF-based systematic solution for the automated co-segmentation of brain PET/CT images into gray matter, white matter and cerebrospinal fluid regions is exposed in [33]. A PET/CT image pair and its segmentation result are modeled as a MRF triplet, and segmentation is eventually achieved by solving a maximum a posteriori (MAP) problem using the expectation maximization (EM) algorithm with simulated annealing. The overall MRF-MAP model was tested both on simulated and real patient PET/CT data. The same authors presented in [34] a more advanced brain PET/CT segmentation model. This dual-modality image segmentation approach converts PET/CT image segmentation into an optimization process controlled

9

simultaneously by PET and CT voxel values and spatial constraints. A modality discriminatory power (MDP) coefficient is applied as a weighting scheme to adaptively combine functional and anatomical information to separate voxels from different tissue types.

The authors of [35] proposed a method for automated delineation of tumor boundaries in whole-body PET/CT by jointly using information from both PET and diagnostic CT images. After an initial robust hot-spot detection and segmentation performed in PET, a model for tumor appearance and shape in corresponding CT structures is learned by weighted non-parametric density estimate. This voxel-based CT classification is then probabilistically integrated with PET classification using the joint likelihood ratio test technique to derive the final segmentation. The algorithm was tested on patient studies with lung and liver tumors identifiable in both the PET and CT images acquired by the same scanner. In this context, a recent study [36] aims at developing a radiomics model from joint FDG-PET and MRI texture analysis for the early evaluation of lung metastasis risk in soft-tissue sarcomas (STSs). The creation of new composite textures from the combination of FDG-PET and MR imaging information, to better identify aggressive tumors, was investigated. The results showed that FDG-PET and MRI texture features could act as strong prognostic factors of STSs.

Yezzi *et al.* [37] introduced a geometric variational framework that uses active contours to simultaneously segment and register features from multiple images. The key aspect of this approach is that multiple images may be segmented by evolving a single contour as well as the mappings of that contour into each image during feature-based realignment steps. The results of three experiments on MRI/CT images of the head and the spine were reported. In [38] a variational segmentation method, based on the minimization of the total variation semi-norm and a convex formulation, was used for segmenting lung tumors and lymph node disease on thoracic PET/CT image pairs, in the context of radiotherapy planning. Also the authors of [39] developed a method based on multi-valued level set deformable models for simultaneous 2D or 3D segmentation of multimodality images consisting of combinations of co-registered PET, CT,

or MRI datasets. In particular, only three patients are considered: a non-small cell lung cancer case with PET/CT, a cervix cancer case with PET/CT, and a prostate patient case with CT/MRI. In addition, CT, PET, and MRI phantom data were used for quantitative validation of the proposed multimodality segmentation approach.

However, we have to focus on PET/MRI joint segmentation approaches reported in the literature. An automatic algorithm for the co-segmentation of HNC based on PET/MRI data was proposed in [40], in order to standardize tumor volume delineation. For both imaging modalities tumor probability maps were derived, assigning each voxel a probability of being cancerous according to its signal intensity. A combination of these maps was subsequently segmented using a threshold level set algorithm. The algorithm processes both the anatomical T2-weighted MRI and FDG-PET data concerning 10 HNC patient datasets acquired by a combined PET/MRI system.

The group led by Bagci and Mollura developed some co-segmentation approaches in multimodal medical imaging, which mostly used random walker (RW) algorithm [29]. In [41] a computer-assisted volume quantification method for PET/MRI dual modality images using automated PET-guided random walk MR image co-segmentation was presented. A small-animal breast cancer model was built by using 30 female nude mice. A more comprehensive and general approach was proposed in [42]. The RW algorithm is extended for jointly delineating multiple objects from multimodal images by unifying graph representation of each image modality in a single product lattice. The overall method results in an automatic and unified framework, providing an automated object detection via interesting uptake region (IUR) algorithm to avoid users having to provide foreground and background seeds. Afterwards, prior to the initiation of the segmentation process, these identified seeds are propagated to the corresponding anatomical images. Although no significant anatomical and functional changes between the scans have to be assumed, the study used PET, PET/CT, MRI/PET, and fused MRI/PET/CT scans (77 studies in all) from 56 patients who had various lesions in different

11

body regions. Finally, a 3D computer-aided co-segmentation tool for lesion detection and quantification from hybrid PET/MRI and PET/CT images was described in [24]. This method used a modality-specific visibility weighting scheme built upon a fuzzy connectedness (FC) image segmentation algorithm.

To the best of our knowledge, this is the first paper that presents a co-segmentation method to integrate MET-PET metabolic information with anatomical MRI in stereotactic neuro-radiosurgery treatments.

The proposed approach aims to properly integrate the two monomodal processing pipeline proposed in [26][28]. Each single method has been already validated in previous journal articles [26][28], comparing each of them against the most common literature segmentation methods. Our method addresses the co-segmentation problem on multimodal PET/MRI only in the brain anatomical district imaging, by exploiting the great sensitivity and specificity of brain MET-PET in distinguishing healthy and pathological tissues. As result, a fully automatic approach was obtained. In FDG-PET studies, target lesions must always be specified by an operator, because healthy structures (such as brain, heart, bladder, and kidneys) normally have high radiotracer uptake [43]. We do not claim that our approach is able to segment other types of imaging data. However, there are no general approaches that can work on all acquisition modalities and in all the clinical contexts without any limitations. As a matter of fact, multimodal PET/CT and PET/MRI segmentation techniques in the literature are quite different and have to be designed *ad hoc*. These methods have to be adapted considering the different imaging acquisition modalities in certain clinical scenarios, and the involved body districts and pathologies.

As concerning state of the art methods on PET/MRI segmentation, we would like to underline that methods based on unifying graphs, which assume no significant anatomical and functional changes between the images acquired using different modalities to directly construct the hyper-graph [21][42] or the sub-graphs with inter-subgraph arcs [31], generally yield a single target

12

volume on the fused multimodal images. Considering a decision-level fusion (i.e. taking into account the physicians' final decision for CTV definition), rather than a feature-level fusion (i.e. processing and fusing the input imaging data into a unifying data-structure) [44], keeps all the initial information even when PET and MR images are considerably different. Especially, the proposed approach yields two different volumes, by processing multimodal PET/MR images:

- the GTV on anatomical MR images, calculated using exploiting the IURs detected on PET images;

- the BTV_{MRI} on PET images, defined by combining the PET dataset with the corresponding MRI GTV segmentation results, so reducing spill-in and spill-out effects between lesion and surrounding tissues.

Thereby, a complete knowledge about the clinical scenario is ensured from both anatomical and metabolic imaging perspectives. It is worth to notice that clinical evaluation is not just a mathematical procedure, based only on tumor area difference or on GTV and BTV union, but a deep decision-making process involving several anatomical and metabolic insights, the specific patient's pathological scenario as well as the physician experience. The CTV identification is actually a critical task accomplished by expert physicians according to tumor volumes (BTV and GTV), and deciding about the regions to be included or excluded in the planned target volume. This can be the basis for personalized therapy, by integrating molecular imaging and allowing for a diagnosis and therapy that is specialized to the individual metabolism and disease [45].

In conclusion, the tackled problem and the aim of the proposed multimodal approach are considerably different with respect to joint segmentation approaches. Employing a decision-level fusion, the assumption of a "ground truth" joint volume, defined on fused multimodal imaging data, and the consequent comparison of the proposed method with related works is not significant, and sometimes misleading. Under these hypotheses, a reference gold-standard for the evaluation is not consistent with the purpose of our work. This retrospective study aims to

evaluate the feasibility and the clinical value of BTV integration in Gamma Knife treatment planning.

3. Materials and Methods

In the current section, firstly PET and MR imaging data concerning the patients are reported, and then our novel fully automatic multimodal PET/MRI segmentation method is described. Lastly, the framework used for the evaluation of the proposed multimodal approach is presented.

## 3.1. Patient Imaging Data

A total of 19 brain metastatic tumors originating from several primary cancers (lungs, breast, kidneys, urothelium, melanoma), undergone stereotactic neuro-radiosurgery, were retrospectively considered in the present study. All the subjects (mean age ± standard deviation: 60 ± 9.80 years; median age: 57 years; age range: 48÷78 years) were treated with Leksell Gamma Knife® model C at Cannizzaro Hospital in Catania, Italy. The patients underwent chemotherapy or radiotherapy to treat primary cancers, before neuro-radiosurgery treatment, so that the T1-weighted MRI sequence alone is not able to perform a clinical differentiation between treatment-related changes and residual tumor after neurosurgery, chemotherapy or radiation therapy [20].

Both MRI and PET datasets were acquired for these subjects. PET and MR imaging data were obtained by two different scanners at two different times. MRI dataset, used for Gamma Knife treatment planning, was scanned a few days after MET-PET study.

Representative instances of input brain MR and PET image pairs are shown in Figure 1.

The research associated with the Leksell Gamma Knife® treatment of brain tumors has no implication on actual patient treatment. No patient information was accessed; therefore,

institutional review board approval was not sought: the proposed image analysis is performed off-line and thus did not change the current treatment protocol.
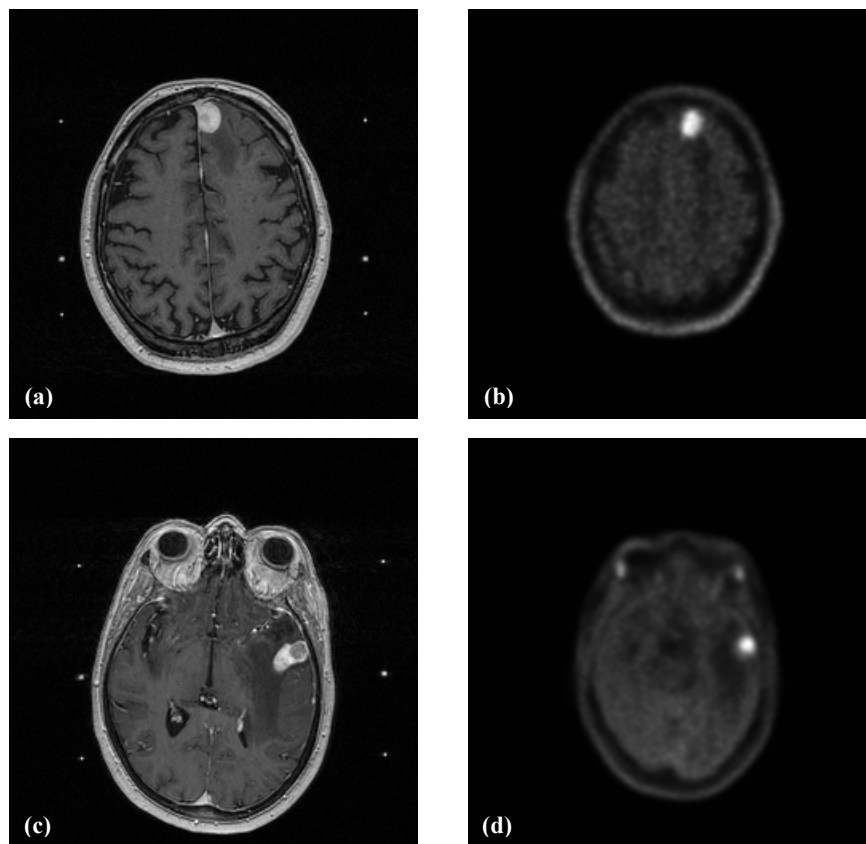
Figure 1 Examples of original input brain MR and PET image pairs concerning patients with brain tumors who underwent Gamma Knife: **(a, c)** MR slices and **(b, d)** the nearly respective corresponding PET slices (metastases #6 and #14). Note the different dimensions and the substantial tridimensional misalignment between corresponding MR and PET images. The images are shown in grayscale.

3.1.1. PET Dataset Description

PET brain acquisitions without head frame were performed using the on time of flight PET/CT Discovery 690 by General Electric Medical Systems (Milwaukee, WI, USA). Patients fasted for 4 hours before PET exam and were intravenous injected with MET. The PET protocol began 10 minutes after the injection. PET images consist of a 256×256 pixel matrix of 1.1719×1.1719×3.27 mm^3 voxel size. Imaging data were encoded in the 16-bit DICOM (Digital Imaging and Communications in Medicine) format.

3.1.2. MRI Dataset Description

All available MRI datasets were acquired on the Gyroscan Intera 1.5T MR Scanner (Philips Medical System, Eindhoven, the Netherlands), before treatment, for the planning phase. MR images were T1-weighted Fast Field Echo ("T1w FFE") contrast-enhanced sequences. MRI acquisition parameters were: TR: 25 ms, TE: 1.808-3.688 ms, matrix size: 256 × 256 pixels, slice thickness: 1.5 mm, slice spacing: 1.5 mm, pixel spacing: 1.0 mm. Therefore, the size of each voxel was $1.0 \times 1.0 \times 1.50$ mm^3. Thanks to the Gadolinium-based contrast agent, brain lesions appeared as enhanced hyper-intense zones. Sometimes a dark area might be present due to either edema or necrotic tissue. Imaging data were encoded in the 16-bit DICOM format.

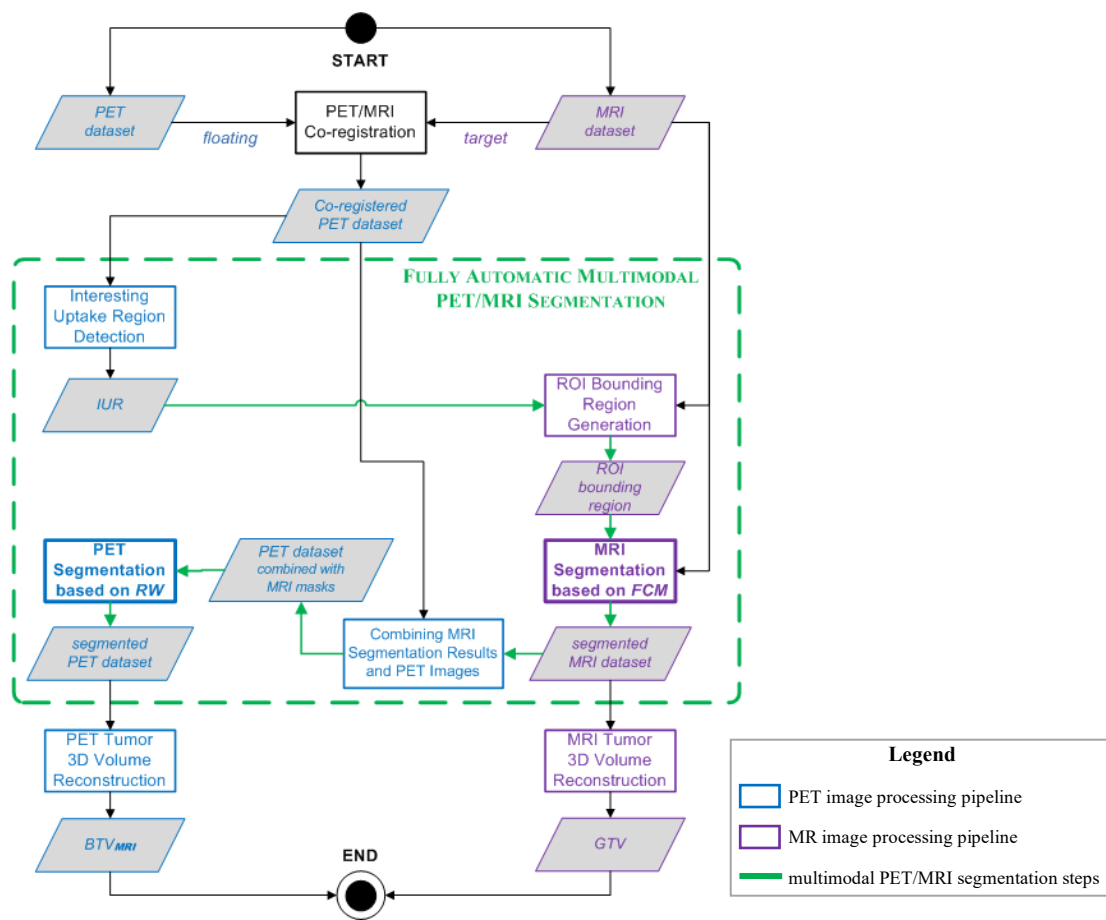## 3.2. The Proposed Multimodal PET/MRI Segmentation Approach

This contribution presents a fully automatic multimodal PET/MRI segmentation approach for Leksell Gamma Knife® treatment planning. The main key novelty is the computation of the BTV_{MRI}, a new BTV that could reduce radioactivity spill-in and spill-out effects considering morphologic GTV information. The proposed method improves and combines two computer-assisted and operator-independent methods previously developed and validated to segment BTV and GTV from PET [22][25][26] and MR [27][28] images, respectively.

These two previous single modality segmentation methods are broadly explained in sections 3.2.1 and 3.2.2, respectively. However, as described in section 3.2.3, an image co-registration stage is mandatory to integrate and quantitatively compare MRI and MET-PET modality imaging data. The proposed fully automatic multimodal PET/MRI segmentation approach is presented in section 3.2.4. Lastly, section 3.2.5 discusses and summarizes parameter setting, by describing the theoretical basis and experiment trials involved in all the parameter value choices.

The main goal is to present a multimodal PET/MRI automatic segmentation method, combining complementary information, and encourage its use in future Gamma Knife treatments.

The proposed method was entirely developed using the MatLab® environment (The MathWorks, Natick, MA, USA). Statistical analysis was performed with the MedCalc® computer program (MedCalc Software, Ostend, Belgium) [46]. Figure 2 outlines the overall flow diagram of the proposed multimodal PET/MRI segmentation method. All the employed parameters were fixed in the proposed computational model for all the analyzed datasets. These settings are completely hidden to the end-users (clinicians), who have not to select any parameters. Therefore, this does not affect the fully automation of the proposed method.

Figure 2 Flow diagram of the proposed fully automatic multimodal PET/MRI segmentation method. The adopted graphical and color notations are explained in the legend box.

3.2.1.   PET Image Brain Lesion Segmentation

BTV segmentation is based on an enhanced RW method. This approach is fully automatic [22]. Briefly, the RW algorithm is able to localize weak boundaries as part of consistent boundaries representing an image as a graph $G = (V, E)$ with nodes (vertices) $v \in V$ corresponding to the voxels and edges (arcs) $e \in E$ are associated to a Gaussian cost function that maps a change in image intensity to the edge weights w_{ij} defined as follows:

$$w_{ij} = \exp\left(-\beta(g_i - g_j)^2\right) \qquad (1)$$

where: g_i and g_j are the image intensity values at voxels i and j, respectively; β is a free parameter. The segmentation problem is to assign a label to unknown nodes, by finding the minimum energy among all possible graph scenarios to achieve an optimal segmentation. The RW method partitions the voxels into foreground and background classes, considering the probability that a "random walker", starting at a source node, first reaches a node with a pre-assigned label visiting every voxel. A probability map is then produced, and a threshold of 50% is chosen to discriminate between foreground and background voxels.

To obtain the BTV delineation, RW parameters have been modulated to incorporate PET information: g_i and g_j have been replaced with the Standardized Uptake Value (SUV) in the voxels i and j. The SUV is the most common semi-quantitative parameter used to estimate radiotracer accumulation within a lesion in clinical practice. It normalizes the voxel activity considering acquisition time, administered activity, and patient's body weight. Hence the PET image is converted in a lattice where the SUV of each voxel is assigned to the corresponding graph node $v \in V$ and the edge weights w_{ij} are computed accordingly.

In addition, to obtain a fully automatic and user-independent method, two crucial improvements have been implemented to overcome two critical issues in the RW methodology:

1. an automatic method to localize starting target and background seeds: the RW algorithm requires a set of pre-labeled seeds, which may be generated by the user, making the RW delineation sensitive to the location of the pre-labeled voxels;

2. a strategy to adaptively determine the appropriate probability threshold rather than fixed one of 50% on the probabilistic output of RW in order to overcome the operator-dependence of the β weighting factor in (1).

A more detailed explanation of these improvements is reported in [22] and [26].

By taking advantage of the great sensitivity and specificity of MET radiotracers in the discrimination between malign versus benign tissues, each brain tumor is independently processed by our algorithm. For each patient study, the highest uptake regions are automatically analyzed. The SUV_{max} value is not global, but is relative to each single brain tumor present in the PET study under examination. Therefore, in the case of n brain tumors a different $SUV_{max}(l_i)$ is identified for each lesion l_i, with $i \in \{1,2,\ldots,n\}$.

Algorithm 1. Iterative procedure for the IUR detection and BTV delineation on PET images

---

1. /* Create an empty list L_{BTV} for storing the coordinates of the voxels included in the segmented brain lesions on the processed PET study */
2. $L_{BTV} \leftarrow \{\}$;
3. /* Initialize the iteration counter for the detected tumors */
4. $i \leftarrow 1$;
5. **do**
6.   Find the slice with the highest $SUV_{max}^{(i)}$ in the PET study, excluding the voxels already in L_{BTV};
7.   /* Check if the $SUV_{max}^{(i)}$ in the i-th iteration is higher than 2.0 (minimum threshold value for considering a candidate region to be a tumor), otherwise stop the loop */
8. **while** ($SUV_{max}^{(i)} \geq 2.0$)
9.   /* Let l_i be the current lesion with $SUV_{max}^{(i)}$, and set the $SUV_{max}(l_i)$ relative to l_i to $SUV_{max}^{(i)}$ */
10. $SUV_{max}(l_i) \leftarrow SUV_{max}^{(i)}$;
11.   /* Segment the current lesion l_i using the Random Walker algorithm */
12. $BTV_i \leftarrow BTVsegmentation(l_i)$;
13.   /* Store the segmented BTV_i voxel coordinates, by updating the list L_{BTV} */
14. $L_{BTV} \leftarrow L_{BTV} \cup getVoxelCoordinates(BTV_i)$;
15.   /* Increment the iteration counter i */
16. $i \leftarrow i+1$;
17. **end**

Accordingly, the iterative procedure for the IUR detection and BTV delineation on PET images can be summarized as in the pseudo-code in Algorithm 1.

At the end of this automatic tumor detection procedure, for a final control on the detected cancer regions, the user can discard any false positive uptake areas.

3.2.2. MR Image Brain Lesion Segmentation

In this section, our preliminary MR brain GTV segmentation approach, based on an unsupervised *Fuzzy C-Means (FCM)* clustering technique and proposed in [27] and [28], is outlined. Nevertheless the method is semi-automatic, operator-dependence is reduced because user intervention is limited only to the selection of a Region Of Interest (ROI) bounding area containing the cancer zone and no parameter setup is required. All the subsequent processing stages are accomplished on the MR images masked with this ROI bounding region.

After pre-processing, *FCM* cluster analysis is performed on MR images including brain tumors. The goal of this algorithm is to classify a dataset $X = \{\mathbf{x}_1, \mathbf{x}_2, ..., \mathbf{x}_N\}$ of N objects (statistical samples represented as vectors belonging to *n*-dimensional Euclidean space $\Re^n$) into C clusters (partitions of the input dataset), represented by C centroids $V = \{\mathbf{v}_1, \mathbf{v}_2, ..., \mathbf{v}_C\}$ [30][47]. A fuzzy partition P is defined as a fuzzy set family $P = \{Y_1, Y_2, ..., Y_C\}$ such that each object can have a partial membership to multiple clusters [48]. The matrix $\mathbf{U} = [u_{ik}] \in \Re^{C \times N}$ defines a fuzzy C-partition of the set X through C membership functions $u_i : X \rightarrow [0,1]$, whose values $u_{ik} := u_i(x_k) \in [0,1]$ represent membership grades of each element $\mathbf{x}_k$ to the ith fuzzy set (cluster) Y_i and have to satisfy the constraints in (2).

$$\begin{cases} 0 \le u_{ik} \le 1 \\ \sum_{i=1}^{C} u_{ik} = 1, \forall k \in [1, N] \\ 0 < \sum_{k=1}^{N} u_{ik} < N, \forall i \in [1, C] \end{cases} \tag{2}$$

Briefly, the sets of all the fuzzy C-partitions of the input X are defined by $M_{fuzzy}^{(C)} = \left\{ \mathbf{U} \in \Re^{C \times N} : u_{ik} \in [0,1] \right\}$. Computationally, *FCM* is an optimization problem where the objective function in (3) must be iteratively minimized using a least-squares method. The fuzziness of the classification process is defined by the weighting exponent *m*.

$$J_m(\mathbf{U},V;X) := \sum_{i=1}^{C} \sum_{k=1}^{N} (u_{ik})^m \left\| \mathbf{x}_k - \mathbf{v}_i \right\|^2 \tag{3}$$

Two clusters are selected ($C=2$) in order to suitably classify a hyper-intense lesion from the healthy part of the brain. In fact, in contrast-enhanced MR brain scans, metastases have a brighter core than periphery and distinct borders distinguishing them from the surrounding healthy brain tissue [49].

As reported in section 3.1.2, the analyzed MR images were T1w FFE contrast-enhanced sequences. Typical MRI protocols, employed in stereotactic radio-surgery treatment planning, include only T1w contrast-enhanced imaging of the head volume. Therefore, no multiparametric MRI structural data (i.e. T1w, T2w, Proton Density (PD), and Fluid Attenuation Inversion Recovery (FLAIR) images) are available and brain tumor segmentation approaches based on multispectral MR images cannot be applied to Leksell Gamma Knife treatment planning. These approaches rely on these multispectral MRI for segmenting and distinguishing cancer enhancement region, necrosis or edema [50].

As a matter of fact, tumor detection and segmentation on contrast-enhanced T1w MRI datasets are based on the hyper-intense enhancement regions. Since sometimes either edema or necrotic material (hypo-intense regions in T1w MR images) could be present in the analyzed tumors, necrosis inclusion in the planned target volume is required for radiosurgery purposes [51]. Therefore, some post-processing steps were designed *ad hoc* to include the necrosis in the planned volume for preventing recurrent cancers, as extensively described in [28].

3.2.3. PET/MRI Modalities Co-registration

An image co-registration stage is mandatory to bring the different MRI and MET-PET datasets, concerning the same patient, into the same space. In this way, it will be possible to make quantitative and meaningful comparisons between the brain lesion segmentation results achieved by both MRI and PET image segmentation methods.

In our multimodality PET/MRI registration, MRI is used as reference image (target) while the PET is the source image (floating), because MRI conveys more anatomical information than PET. Indeed, PET imaging is characterized by weak boundaries and has a lower spatial resolution than MRI. Realignment and reslicing operations are thus required to get a one-to-one mapping between PET and MRI slices. From an algorithmic perspective, image co-registration involves finding parameters (i.e. geometric transformation matrix) that either maximize or minimize some objective function. However an accurate interpolation method is clearly required, by which the floating and target images are sampled when being represented in different spaces [52][53].

PET/MRI inter-modal 3D registration was performed using *SPM 12* (*Statistical Parametric Mapping*, Wellcome Trust Centre for Neuroimaging, University College, London, UK), a software package designed for the analysis of brain imaging data sequences [54]. We relied on the *SPM* tool that is widely used in the neuroimaging community and in the clinical routine, also for Voxel-Based Morphometry (VBM).

The registration method used by *SPM* is based on the work by Collignon *et al.* [55], where the original interpolation method has been changed to give a smoother cost function. The images are also smoothed slightly, by means of their histogram. This makes the cost function as smooth as possible, to give faster convergence and less chance of local minima. A 3D rigid-body model, parameterized by 3 translations and 3 rotations about the different axes, is used by means of voxel-to-voxel affine transformations. This approach is very efficient for brain anatomical district.

We chose Normalized Mutual Information (NMI) as the cost function to be optimized. The Mutual Information registration criterion states that the mutual information of the image intensity values of corresponding voxel pairs is maximal if the images are geometrically aligned. Mutual Information is the most intensively investigated criterion for registration of intra-individual human brain images [56][57]. In addition, PET/MRI registration misalignment can be large with respect to the field of views, then a criterion invariant to image overlap statistics is very important, such as the NMI [58].

Since MET-PET and MRI multimodal images are written in a different space, an efficient resampling and interpolation method must be utilized. Although Nearest-Neighbor and Trilinear interpolations are faster, it may be better to use a higher degree approach to achieve more accurate results (i.e. reducing the deviation from an ideal low-pass filter, by avoiding artifacts mostly near edges) [59]. In particular, we used the 4th Degree B-Spline interpolation.

Two instances of PET/MRI co-registration are shown in Figure 3, where the quality of the achieved registration can be qualitatively appreciated with the checkerboard images (Figure 3(a) and (d)) as well as fused PET/MR images (Figure 3(b) and (e)). In addition, the joint histogram, that is a feature space constructed by counting the number of times a combination of gray values occurs contextually on source (MET-PET) and reference (MRI) images, was also computed and plotted (Figure 3(c) and (f)). Along the axes of each joint histogram the gray values of the two images are represented: from left to right for source (MET-PET) and from bottom to top for reference (MRI). Original and final joint histograms prove the quality of the Normalized Mutual Information registration process, because pixel values are mainly redistributed on the histogram diagonal.

3.2.4. Fully Automatic Multimodal PET/MRI Segmentation

In the following, a thorough explanation of the various processing steps that make up the proposed fully automatic multimodal PET/MRI segmentation method is presented. In the flow

diagram shown in Figure 2, for a better understanding, PET and MR image processing pipelines are represented with blue and purple blocks, respectively. It is worth noting, the smart combination of the two single modality pipelines (green connections in Figure 2). In particular, PET and MRI segmentation results mutually exploit each other. Firstly, the IUR, obtained on co-registered PET images by the graph-based tumor segmentation method (see section 3.2.1), is used for the generation of an area including the tumor ROI on MR brain images. These ROI bounding regions are calculated adaptively on MR images using a Level Set method and then utilized by the MRI brain lesion segmentation method based on FCM clustering technique (see section 3.2.2). Lastly, MRI GTV masks are combined with PET images, which are processed by the RW algorithm, to influence and refine BTV segmentation on PET images.
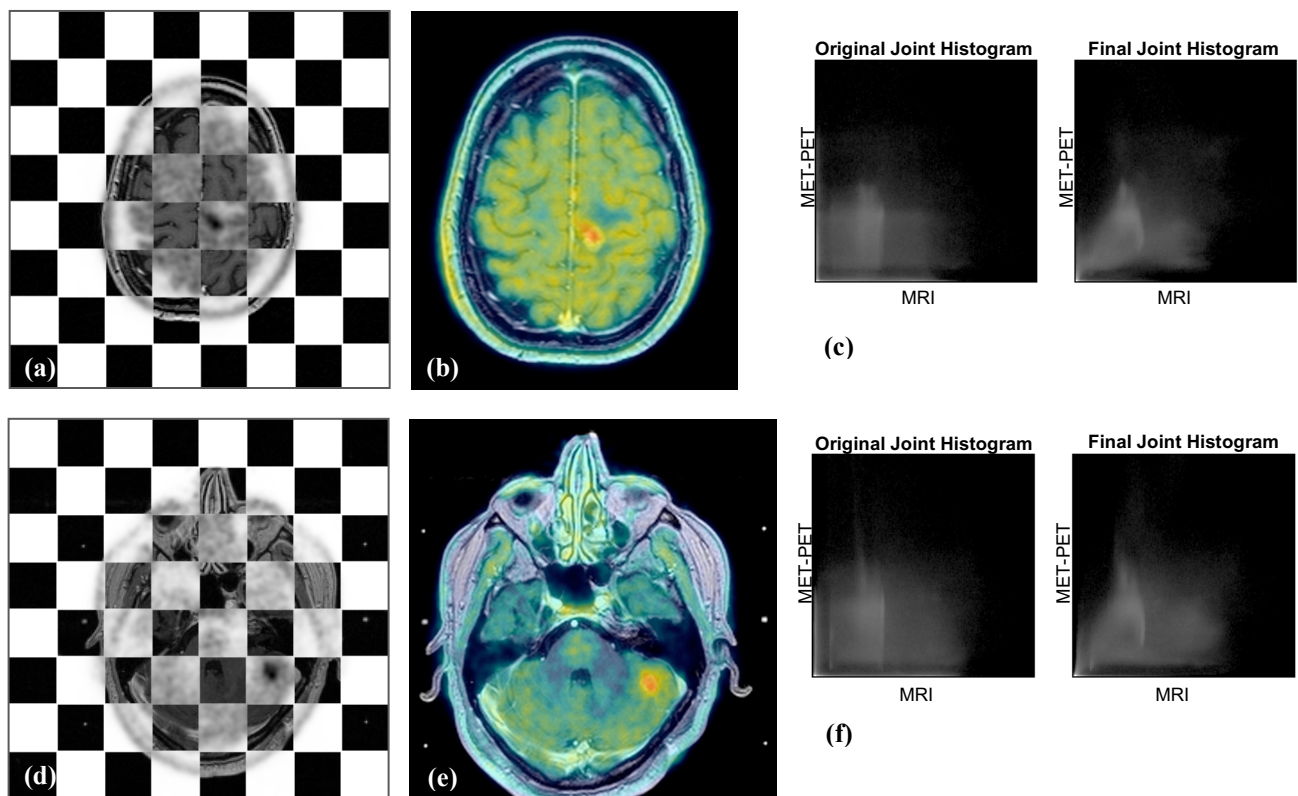
Figure 3 Instances of PET/MRI co-registration using *SPM* via maximization of Normalized Mutual Information (tumors #7 and #10): **(a, d)** checkerboard images of co-registered PET (negative grayscale) and MRI (normal grayscale); **(b, e)** fused images (MRI in grayscale and PET in Jet colormap); **(c, f)** corresponding original and final joint histograms (feature space constructed by counting the number of times a combination of gray values occurs contextually on MRI and MET-PET images) for (b) and (e), respectively.

3.2.4.1. Interesting Uptake Region Detection

The fully automatic multimodal PET/MRI segmentation starts with the automatic identification of the PET slices with the maximum SUV (SUV_{max}), relative to each lesion detected by means of the iterative procedure reported in section 3.2.1, on PET dataset previously co-registered with the corresponding MRI (see section 3.2.3). The voxels with a SUV greater than 95% of the SUV_{max} concerning each tumor are marked as target seeds. The neighborhood of the node with SUV_{max}, through searching in all 8 directions, is explored to identify the voxels with a SUV less than 30% of the average of target seed SUVs [26]. In this way, 8 background nodes are identified. Once the foreground and background seeds are automatically localized, the PET lesion is segmented using our enhanced RW method (see section 3.2.2): the probability threshold to discriminate between target and background voxels is obtained slice by slice to follow the whole lesion volume. In this way, the method takes into account the intensity gradient and contrast changes of the metabolic lesion over the entire range of PET slices. Once the BTV has been extracted, the ROI of the PET slice with the SUV_{max} is propagated to the corresponding MRI dataset. In addition, the range of segmented PET slices with high uptake regions is also provided to the next processing phase, to generate efficiently a ROI bounding region for the tumor on MR images (see the following section 3.2.4.2). Such information defines the so-called Interesting Uptake Region (IUR).

3.2.4.2. ROI Bounding Region Generation

A coarse lesion delineation on MR images is required in order to define automatically a bounding region that encloses the actual GTV on MR slices. Hence user interaction, needed by the methods in [27][28] through a ROI selection tool, will be completely prevented and avoided. Because of the variability of brain lesions in terms of location and intensity values, the definition of a valid ROI bounding region is not a trivial problem. A bad choice of the ROI bounding region on MR image can affect the whole FCM clustering process. Therefore, this

task must be carried out not in a static way (e.g. using a simple morphological dilation or closing with a fixed structuring element [60]), but rather dynamically by processing MRI input data.

This adaptive procedure starts on the lesion ROI found on SUV_{max} slice, as described in section 3.2.4.1. This IUR is first dilated (using a structuring element represented by a disk of 3 pixel radius) and then utilized as a binary step function to initialize a Level Set method. A rough and over-estimated MRI brain lesion segmentation, based on the Distance Regularized Level Set Evolution (DRLSE) formulation proposed in [61], is used to generate dynamically a bounding region that includes the brain lesion in the MR slice corresponding with the SUV_{max} PET slice. Unlike Region Growing algorithm [62], DRLSE method allows a controlled and regular Level Set Function (LSF) evolution, by avoiding leaking in the brain tissue area. In short, Level Set methods represent an active contour as the zero level set of a higher dimensional function, i.e. a time dependent LSF $\phi(x, y, t)$, and determine the evolution of the contour [63].

Let $\phi : \Omega \to \Re$ be a LSF defined on a domain Ω, the energy functional is defined by (4):

$$E_{\varepsilon} := \mu R_p(\phi) + \lambda L_g(\phi) + \alpha A_g(\phi) \tag{4}$$

where:

- $\mu > 0$, $\lambda > 0$ and $\alpha \in \Re$ are the coefficients of the energy functional terms R_p, L_g and A_g, respectively;

- $R_p(\phi) := \mu \int_{\Omega} p(|\nabla \phi|) d\mathbf{x}$ is the level set regularization term, where $p:[0,+\infty) \to \Re$ is a potential function. In order to smooth the LSF effect and ensure accurate computation for curve evolution by maintaining the signed distance property $|\nabla \phi| = 1$, a potential function $p(s)$ with a minimum point at $s = 1$ is chosen. In particular, a double-well potential, with two minimum points at $s = 0$ and $s = 1$, was used: $p(s) = \begin{cases} (1/(2\pi)^2)(1 - \cos(2\pi s)) & \text{if } s \leq 1 \\ (1/2)(s-1)^2 & \text{if } s > 1 \end{cases}$;

- $L_g(\phi) := \lambda \int_\Omega g \delta(\phi) |\nabla \phi| \, d\mathbf{x}$ is an energy functional that computes the line integral of the edge

  indicator function $g = \frac{1}{1+|\nabla G_\sigma * I|^2}$ (G_σ is a Gaussian kernel with standard deviation σ that is

  convolved with the image $I \in \Omega$ to reduce the noise) along the zero level contour of ϕ with

  the Dirac delta function δ;

- $A_g(\phi) := \alpha \int_\Omega g H(-\phi) \, d\mathbf{x}$ is an energy functional that calculates weighted area of the region

  $\Omega_\phi^- = \{\mathbf{x} : \phi(\mathbf{x}) < 0\}$. This term is introduced to speed-up the motion of the zero level contour in

  the LSF evolution process, which is necessary when the initial contour is far away from the

  desired object boundary. Lastly, H is the Heaviside step function, whose derivative is the

  Dirac delta function δ.

In practice and for implementation purposes, as described in [64], the Dirac delta function δ

and Heaviside step function H in the functional in eq. (3) are approximated by their respective

smooth version δ_ε and H_ε, defined as:

$$\delta_\varepsilon(x) = \begin{cases} \frac{1}{2\varepsilon}\left(1 + \cos\left(\frac{\pi x}{\varepsilon}\right)\right) & \text{if } |x| \le \varepsilon \\ 0 & \text{if } |x| > \varepsilon \end{cases} \tag{5}$$

$$H_\varepsilon(x) = \begin{cases} \frac{1}{2}\left(1 + \frac{x}{\varepsilon} + \frac{1}{\pi}\sin\left(\frac{\pi x}{\varepsilon}\right)\right) & \text{if } |x| \le \varepsilon \\ 1 & \text{if } x > \varepsilon \\ 0 & \text{if } x < -\varepsilon \end{cases} \tag{6}$$

where ε (usually set to 1.5) is a parameter that specifies the width of the Dirac delta function

and the slope of the Heaviside step function.

The overall energy functional in (4) can be minimized, given an initial LSF $\phi(\mathbf{x},0) = \phi_0(\mathbf{x})$, by

solving the following gradient flow (7) in the temporal variable $t \in [0,+\infty)$:

$$\frac{\partial \phi}{\partial t} = \mu \, \mathrm{div}\left(d_p\left(|\nabla \phi|\right)\nabla \phi\right) + \lambda \delta_\varepsilon(\phi)\mathrm{div}\left(g\frac{\nabla \phi}{|\nabla \phi|}\right) + \alpha g \delta_\varepsilon(\phi) \tag{7}$$

27

where $\mathrm{div}(\cdot)$ is the divergence operator and the function d_p, defined as $d_p = p'(s)/s$, has a

diffusion effect on the LSF. In particular, in our approach, we used $\phi_0(\mathbf{x}) = \begin{cases} -c_0 & \text{if } \mathbf{x} \in IUR_0 \\ c_0 & \text{otherwise} \end{cases}$,

where $c_0 > 0$ is a constant and $IUR_0 \in \Omega$ is the initial IUR given by the processing steps

described in section 3.2.4.1. Therefore, the utilized LSFs take negative values inside the zero

level contour and positive values outside. This choice causes the coefficient α to take negative

value to expand the active contour. The DRLSE and the temporal partial derivative $\partial\phi/\partial t$ were

implemented as a finite difference numerical scheme using a time step Δt.

Eq. (7) is an edge-based geometric active contour model and represents an application of the

general DRLSE formulation. This variational formulation demonstrates good adaptation

segmentation results in different image processing contexts, thanks to the available free

parameters.

Three examples of ROI bounding regions delineated, on original MR images, by the DRLSE-

based method are shown in Figure 4(a-c).

These computations are performed just once for each dataset. In fact, only one bounding region

is determined via DRLSE-based segmentation and it is extruded along the *z* axis onto the other

candidate MR slices. For this purpose, the range of PET slices with high uptake regions is also

provided by the IUR detection steps (see section 3.2.4.1), to construct a cylindroid (i.e. a

cylinder with irregular-shaped bases) including the whole GTV brain lesion. Since PET and

MRI tumor volumes may be distributed along different axial slices, the range of PET active

slices is augmented by three slices on upper and lower sides, in order to ensure the total

enclosing of the tumor into the cylindroid defined on the MRI dataset.

Figure 4(d) shows 3D volume rendering of the cylindroid extruded on the ROI bounding region

shown in Figure 4(a). The whole GTV is included into the cylinder volume (see Figure 4(e)).
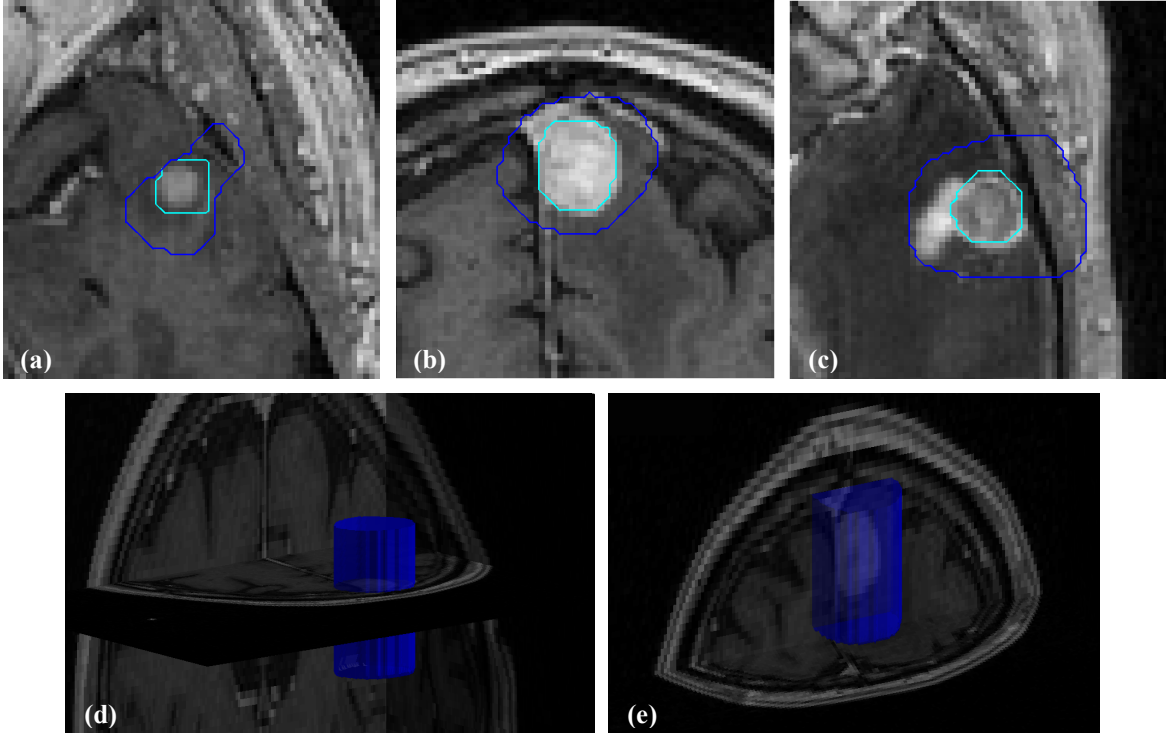
Figure 4 ROI bounding region generation on MR images: **(a, b, c)** three examples (tumors #5, #6, and #10) of bounding region (blue contour) determined via DRLSE-based method, starting from IUR (cyan contour) imported from the corresponding SUV_{max} PET slice. Cylindroid extrusion on MRI dataset according to active PET slice range: **(d)** tridimensional bounding cylindroid for the tumor in the temporal brain lobe, reported in **(b)**, rendered with transparent blue surface (Alpha Blending with $\alpha = 0.70$) on 3D orthogonal tri-planar view (middle slice is shown in the axial plane), that includes the whole GTV, as visible in **(e)**.

3.2.4.3. MRI Segmentation based on the FCM Algorithm

As stated before in section 3.2.2, brain GTV segmentation on MR images is accomplished using our validated semi-automatic method described in [27][28]. However, due to the automation of the segmentation process, the direct control of the human operator is lost during ROI bounding region manual delineation. Some MR images included in the extruded cylindroid (defined by the steps in section 3.2.4.2), especially the most distant slices from the IUR, might include no brain tumor as well as anatomical parts with pixel values similar to enhancement regions (such as bone or epidermal tissue).

For the former case, our MRI brain lesion segmentation method yields an empty ROI. For the latter case, a shape-based control on connected-components belonging to the cluster with the highest intensity pixels is also defined, by taking advantage of the pseudospherical appearance of metastatic brain tumors [49]. When either skull bone or skin are included in the ROI bounding region, since IUR is located near brain boundary, other high-valued pixel areas may be erroneously segmented by the unsupervised FCM clustering algorithm. These areas are often characterized by a lengthened shape and may be removed by checking eccentricity (ratio between the foci distance related to an ellipse and its own major axis length) and extent (ratio between the pixels of the region and the bounding-box pixels) of the connected-components. Theoretically suitable and experimentally validated feature values for this refinement step are:

$$\begin{cases} \text{Extent} \geq 0.6 \\ 0.0 \leq \text{Eccentricity} < 0.8 \end{cases} \tag{8}$$

Figure 5 shows segmentation results on the images reported in Figure 4. In particular, refinement steps can be appreciated in Figure 5(c), where the region composed of the skin highest pixels included in the ROI bounding region is correctly removed by the shape-based controls (yellow boundary).
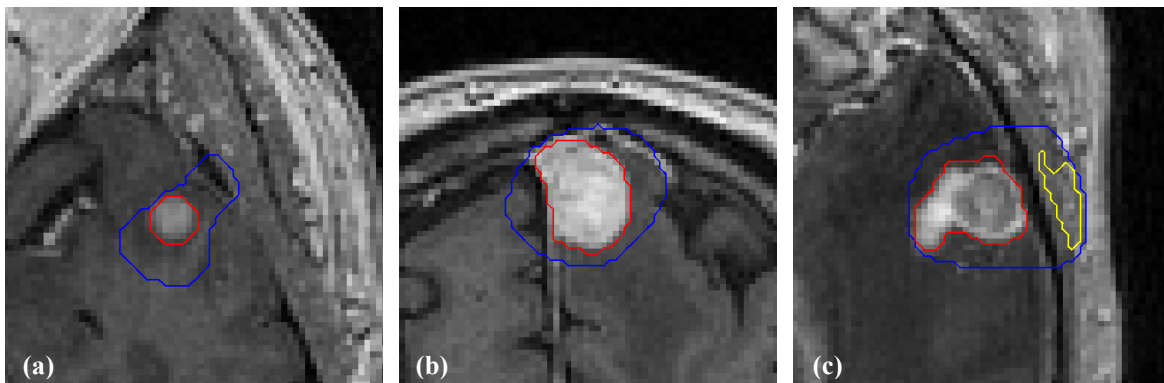
Figure 5 Examples (tumors #5, #6, and #10) of brain GTV segmentation on MR images (red contour), starting from the ROI bounding region (blue contour). A difficult case is shown in **(c)**, where a lengthened hyper-intense region of the head skin is detected by FCM clustering (yellow contour), but it is removed using the shape-based control.

Although the literature offers 3D approaches for brain lesion segmentation [65], we chose a 2D methodology because 3D *FCM* should be not well suitable on clusters with more general shapes [66]. The analyzed brain tumors are composed of inhomogeneous cancerous tissue and necrotic material. As a matter of fact, tumor detection and segmentation on contrast-enhanced T1-weighted MRI datasets are based on the hyper-intense enhancement regions. Sometimes a dark area might be present due to either cystic or necrotic tissue, which must be included into the GTV for radiotherapeutic purposes. These hypo-intense areas can negatively affect the *FCM* clustering process when 3D MRI data are processed. In these cases, clustering could yield several disconnected volumes and successful post-processing steps are very difficult. On the other hand, performing *FCM* cluster analysis on the single MRI slices is definitely more reliable and post-processing steps proposed in [27][28] are able to segment the whole tumor.

3.2.4.4. Combining MRI Segmentation Results and PET Images

Lesion segmentation results on the morphologic brain MRI data, obtained according to section 3.2.4.3, are combined with the metabolic information of the co-registered PET images. This PET dataset represents the input of the RW algorithm. In this way, MRI GTV is utilized to combine the superior contrast of PET images with the higher spatial resolution of MR images.

Each PET slice is weighted pixel-by-pixel according to the corresponding MRI ROIs. Nevertheless, an assumption that there is a one-to-one correspondence between BTV and GTV is unrealistic. Lesions may have smaller uptake regions compared to GTV, such as shown in Figure 6(c) and Figure 7(c). In the same way, the PET lesion can show additional area compared to lesion boundaries in MR images (see Figure 7(d) and Figure 8(c)).

For this reason, we incorporate, with extreme caution, the MRI GTV binary mask in the RW-based segmentation procedure. In particular, PET pixels inside the corresponding MR target are multiplied by a gain factor to slightly emphasize probable lesion area; PET pixels outside the corresponding MRI ROIs are weakly underestimated in order to reduce radioactivity spill-in

effect, from background into the lesion, and spill-out effect, from the lesion into background, by taking advantage of the higher spatial resolution of MR images [67].

3.2.4.5. PET Segmentation based on the RW Algorithm

The RW-based segmentation process on the input PET dataset, described in section 3.2.1, is updated and repeated, in the same way, on the same PET dataset combined with the corresponding MRI GTV binary masks (see previous section 3.2.4.4) in order to achieve a new BTV, in this paper also called as BTV_{MRI}.

In PET imaging, the adaptive probability threshold is computed separately slice-by-slice to follow the whole lesion volume, by taking into account the intensity gradient and contrast changes of the metabolic lesion over the entire range of PET slices. This key feature could be lost using a fully 3D method: the proposed method is then performed in parallel for the slices adjacent to the starting PET slice with the SUV_{max} [26].

3.2.5. Parameter Setting

In our target volume validation experiments, the following parameter setting was empirically employed for all analyzed brain cancer datasets, always according to a theoretical basis.

For the BTV segmentation in PET, regional information based on the SUV thresholding plays a key role. In particular, the 30% and 95% thresholds of the SUV_{max} used to find the background and target seeds are those which minimize the differences between actual and PET volumes in phantom experiments as reported in [26]. Especially, the threshold ranged from 10% to 40% and from 70% to 95% (with a step size of 5% in both cases) for background and target seeds, respectively. In the case of multiple brain tumors, the IUR detection and BTV delineation iterative procedure ends when the SUV_{max} of the currently processed lesion is less than 2.0 [g/mL], to avoid the detection of non-tumor structures with moderate uptake. For all the analyzed brain tumors, the SUV_{max} range is 2.580 ÷ 6.828 [g/mL], with a mean value of 4.149 [g/mL] and a standard deviation of 1.360 [g/mL].

32

In the GTV segmentation on MR images, the bounding region is generated using the LSFs (see section 3.2.4.2). Although the DRLSE framework is characterized by several parameters [61], the proposed multimodal segmentation process is not too sensitive to the choice of these values. In our implementation, relying on the theoretical basis and experimental findings in [61], we set the parameters accordingly and tested them carefully.

As reported in Li *et al.* [61], the DRLSE model is not sensitive to the choice of λ and μ, which can be fixed for most of applications. Especially, we used $\mu = 0.2$ and $\lambda = 5$.

It is worth to note that the parameter α needs to be carefully tuned. A nonzero value forces the motion of the contour, but the resulting final contour may slightly deviate from the true object boundary due to the shrinking or expanding effect of the weighted area term. To avoid this, the final contour can be refined by further evolving the contour for a few iterations with $\alpha = 0$ (e.g. 10 iterations). Since an over-estimated segmentation is required to define a ROI boundary region on MR images and we deal with weak object boundaries, a large value of α may cause boundary leakage, i.e. the active contour can easily pass through the object boundary. For this reason, a relatively small α was chosen to reduce boundary leakage. We used a binary step function with $c_0 > 0$ as initial LSF, consequently the utilized LSFs take negative values inside the zero level contour and positive values outside. This choice causes the coefficient α to take negative value to expand the active contour. For these reasons, we used $\alpha = -1.0$. Moreover, the constant c_0 controls the width of the Signed Distance Band (SDB), because ϕ is a signed distance function in the SDB and its values vary in the range $[-c_0, c_0]$. Since the image domain is a discrete grid and the SDB should have at least one grid point on each side of the zero level contour, it is suggested to choose $c_0 \geq 1$. During our experiment trials, the value $c_0 = 3$ has provided satisfying results for the generation of the ROI bounding region. A Gaussian kernel with standard deviation $\sigma = 0.8$ in the edge indicator function g in (4) represents an effective solution for image noise reduction. Finally, to achieve a good compromise between computation

time and numerical accuracy. the value $\Delta t = 1.0$ is a good choice, because the DRLSE model allows to use large time steps to significantly reduce the number of iterations.

In conclusion, considering our experimental trials (for all the different MRI datasets), the multimodal segmentation process is not too sensitive to the choice of these values. As a matter of fact, LSF-based segmentation is used just to yield a first rough and over-estimated segmentation to generate a ROI boundary region for the GTV segmentation, by adapting on the current processed MR images.

The constraints defined in (8) were also validated experimentally. These properties can be associated to each region and considered together define a selective checking about pseudospherical shapes. Especially, the values in (8) were selected by computing these properties for each MRI cancer slice during the GTV experiment trials on the 19 tumors considered in this study. For a further analysis, we validated the joint condition in (8) on 11 other tumors, concerning independent MRI datasets acquired by another institution (University Hospital "Paolo Giaccone", Palermo, Italy) with a Signa HTxt scanner (General Electric Medical Systems, Milwaukee, WI, USA) using a T1-weighted contrast-enhanced protocol (voxel size was $1.04 \times 1.04 \times 1.20$ mm^3). The achieved values satisfied the joint condition in (8) and were consistent also with independent datasets, showing a reproducible behavior of the extent and eccentricity properties calculated on a total of different 30 tumors. These experimental findings show that the chosen parameter values are not over-fitted and generalize well also when new MRI datasets are processed.

In the BTV$_{MRI}$ segmentation process, which combines MRI segmentation results and PET imaging (section 3.2.4.4), two factors were used: the former to emphasize MR tumor area (i.e. gain factor) and the latter to reduce the radioactivity spill-in and spill-out effects. The clinical staff evaluated the 15% and 5% values, respectively, as the best among those analyzed in 5 patient cases: the values ranged from 5% to 50% and from 5% to 30% (with a step size of 5% in both cases), respectively.

3.3.   Evaluation Metrics

In this section, a framework for the evaluation of multimodal PET/MRI segmentation is presented. Overlap-based and spatial distance-based metrics are considered to measure similarity and correlation concerning PET and MRI segmentation approaches. Assuming PET and MRI segmentations as two different processes, the evaluation metrics were computed according to the formulations presented in [68] and [69]. In fact, the aforementioned empirical discrepancy methods (supervised evaluation metrics) are intended to determine the accuracy achieved by a computer-assisted segmentation method against a gold-standard (manual segmentation performed by an expert) [70]. However, these formulations may be suitably generalized to quantify the similarity and correlation between two different segmentation procedures on images defined on the same space (i.e. the same image or co-registered images). Finally, a qualitative assessment, using a Likert scale, was carried out by experienced clinicians to evaluate retrospectively the clinical value of BTV integration in Gamma Knife treatment planning.

Although spatial overlap-based and distance-based metrics generally quantify the segmentation accuracy against a gold-standard, in this paper the above metrics are used for measuring the similarity as well as the differences among the extracted volumes (i.e. GTV, BTV and BTV_{MRI}) and also to highlight that the metabolic and anatomical volumes are so different to justify a CTV that takes into account both MR and PET imaging.

3.3.1.   Spatial Overlap-based Metrics

Our aim is to demonstrate that PET and MR imaging convey different information. For this purpose, similarity and correlation measures were considered. Assuming PET and MRI segmentations as two different processes, several metrics were included in our quantitative assessment, by adapting formulations based on a gold-standard, as in [68][69].

Let BTV and GTV be the results achieved by the PET and MRI 3D segmentation approaches, respectively. Each segmentation result has to be seen as a set of samples composed of pixels in 2D or voxels in 3D.

Dice similarity coefficient (DSC) is the most used statistic measure for comparing the similarity of two segmentation processes, and it is defined in (9):

$$DSC = \frac{2\,|BTV \cap GTV|}{|BTV| + |GTV|} \times 100\%$$

(9)

3.3.2. Spatial Distance-based Metrics

Although overlap-based metrics are very powerful for measuring the similarity between two image segmentation procedures, they are highly susceptible to differences between the positions of segmented volumes and highly dependent on their own size. Hence, to take into account the spatial position of the voxels, distance-based metrics are highly recommended. In particular, they must be utilized when the boundary delineation (contour) of the segmentation is critical, such as in target delineation for radiation therapy.

Thus, it is required to quantitatively estimate the spatial distance between the 3D volume boundaries computed by the PET and MRI segmentation methods, which are formally represented by the vertex points $A = \{\mathbf{a}_i : i = 1,2,\ldots,N\}$ and $B = \{\mathbf{b}_j : j = 1,2,\ldots,M\}$, respectively.

The Hausdorff distance (HD) between the point sets A and B is a max-min distance defined by:

$$HD = \max\{h(A,B), h(B,A)\}$$

(10)

where $h(A,B) = \max_{\mathbf{a} \in A}\left\{\min_{\mathbf{b} \in B}\left\{\|\mathbf{a} - \mathbf{b}\|\right\}\right\}$ is called the directed Hausdorff distance and

$\|\mathbf{a} - \mathbf{b}\| = \sqrt{\sum_{k=1}^{n}(a_k - b_k)^2}$ is a norm (in our case, the Euclidean distance defined on n-dimensional

Euclidean space $\Re^n$ is used) [71].

Since medical images are usually characterized by noise and the *HD* is generally sensitive to outliers, a more stable distance formulation must be also considered. The average distance (*AVD*), that is the *HD* averaged over all points in *A* and *B*, is defined by:

$$AVD = \max\{d(A,B), d(B,A)\} \tag{11}$$

where $d(A,B) = (1/N)\sum_{\mathbf{a}\in A}\min_{\mathbf{b}\in B}\|\mathbf{a}-\mathbf{b}\|$ is the directed average distance [68].

Lastly, in order to take into account the correlation of all samples belonging to two different points clouds, a variant of the Mahalanobis distance (*MHD*) is used. Again, let *BTV* and *GTV* be the set of voxels segmented by PET and MRI segmentation methods, respectively. The *MHD* between *BTV* and *GTV* is:

$$MHD = \sqrt{(\mu_{BTV} - \mu_{GTV})^T \Sigma^{-1}(\mu_{BTV} - \mu_{GTV})} \tag{12}$$

where μ_{BTV} and μ_{GTV} are the means of the two 3D segmentations. Furthermore, Σ is the common covariance of the two sets and is given by $\Sigma = \dfrac{|BTV|\Sigma_{BTV} + |GTV|\Sigma_{GTV}}{|BTV| + |GTV|}$.

3.3.3. Clinical Evaluation

The proposed method computes the tumor volumes defined in MRI as well as in MET-PET, simultaneously. Two boundaries are separately generated: one on MRI (i.e. GTV) and one on PET (i.e. BTV or BTV$_{MRI}$). Ideally, both GTV and BTV should be validated against a manual delineation by the experts, considered as our "ground truth", using the same PET/MRI datasets. However, due to the current clinical protocol in Leksell Gamma Knife treatment planning, the manual reference contours are available either on MR or PET images only, but not on the fused PET/MR images. Currently, it is not possible to define a real "gold-standard" CTV according to both morphologic MRI and metabolic PET images without treatment response evaluation, since the treatment is planned on MRI datasets alone in the clinical practice. As a matter of fact, ground truth refers to having exact knowledge of the tumor size.

In PET imaging, and consequently in multimodal PET/MR imaging, the metabolic ground truth is impossible to be obtained for images concerning living humans. Thus, the validation of PET methods with real patient images lacks of an actual gold-standard. In addition, manual delineation by expert physicians is subject to intra- and inter-operator variability, especially in tumor segmentation on PET images. Histological images provide the only valid ground truth for quantitative segmentation evaluation in human studies. Obviously, the histology of brain metastases treated using neuro-radiosurgery is unavailable. For this reason, the proposed monomodal PET image segmentation method was assessed using phantom experiments [26]. The same algorithm has been already applied in a real clinical environment to assess the clinical feasibility of the proposed automated approach [26].

So, to assess the clinical utility and feasibility of the proposed multimodal method and to evaluate retrospectively the clinical impact of BTV integration in Gamma Knife treatment planning, a qualitative evaluation, using a five-point Likert scale ranging from 1 (worst) to 5 (best), was carried out by a team of experienced physicians.

The clinical staff, composed of a neurosurgeon, a nuclear medicine physician, and a radiation oncologist, jointly analyzed the brain tumors without any information of the used segmentation method (BTV or BTV$_{MRI}$). By comparing their perspectives by different clinical backgrounds, the physicians were able to gain insights about the tumors and provide a more careful evaluation for each case. As a matter of fact, a Likert scale, rather than providing fixed criteria, allows clinicians to give a score based on overall impression, focusing mainly on the clinical value of BTV in an accurate treatment planning.

Although possibly prone to greater inter-observer variability, this approach may be more familiar to some physicians and may perhaps be more straightforward to apply for observers with previous experience in brain PET imaging.

The used Likert scale, according to retrospective clinical value for treatment planning, was defined as:

1. strong worsening in CTV definition;

38

2. moderate worsening in CTV definition;

3. indifferent, neither enhancement nor worsening in CTV definition;

4. moderate enhancement in CTV definition;

5. strong enhancement in CTV definition.

4. Results

The evaluation of the data presented in this study was performed retrospectively on 19 metastatic brain tumors, treated with Leksell Gamma Knife. Nowadays, the clinical protocol does not usually consider co-registered PET images for Gamma Knife treatment planning.

In the proposed multimodal segmentation approach, two different PET segmentation results were computed: (i) BTV, by considering PET images alone (section 3.2.4.1), and (ii) BTV_{MRI}, by considering PET/MRI co-segmentation (section 3.2.4.4). Therefore, BTV and BTV_{MRI} can be used interchangeably in Eqs. (9)-(12), depending on the usage context.

Firstly, volumes measured on PET and MRI data are reported and, for a quantitative assessment, PET/MRI volume difference and centroid distance were calculated for each lesion.

Figure 6(a) and (c) show experimental results achieved by the proposed multimodal PET/MRI segmentation method on the input image pairs reported in Figure 1(a, b), and Figure 1(c, d), respectively. In addition, the corresponding GTV and BTV$_{MRI}$ volume rendering is reported in Figure 6(b) and (d), respectively.
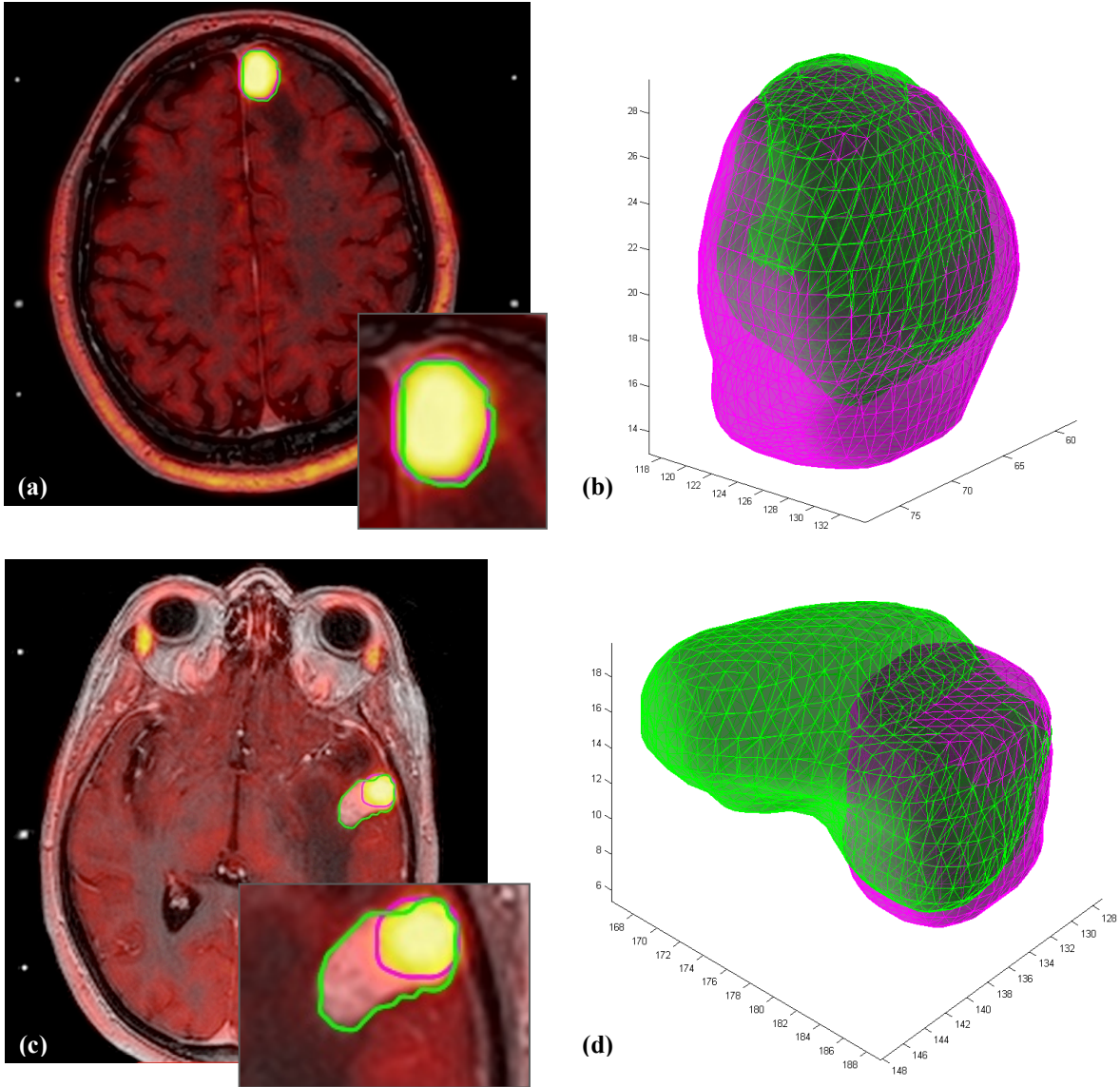
Figure 6 Results achieved by the proposed multimodal PET/MRI segmentation method on the input image pairs (metastases #6 and #14) reported in Figure 1(a, b) and Figure 1(c, d), respectively. The BTV$_{MRI}$ (magenta contour) and GTV (green contour) are superimposed: **(a)** boundaries computed on PET and MR images are nearly overlaid; **(c)** the two ROIs are very different in this case. At the bottom right, the lesion regions are zoomed in both cases. Tridimensional volume reconstructions of brain tumors in (a) and (c) are shown in **(b)** and **(d)**, respectively. Transparent surfaces are rendered with Alpha Blending ($\alpha = 0.50$) to emphasize volume intersections.

Three other interesting examples obtained by the proposed multimodal segmentation method can be visually and qualitatively evaluated in Figure 7.

40

It is worth to observe that the margin of enhancement of tumors in MRI datasets is not always strongly correlated with high uptake regions in PET images. Segmentation results of PET images combined with GTV MRI masks are very stable (magenta boundaries in Figure 7), even if GTV is quite different. In Figure 7(d), Partial Volume Effect (PVE) on PET image [67] is reduced by using MRI ROIs.
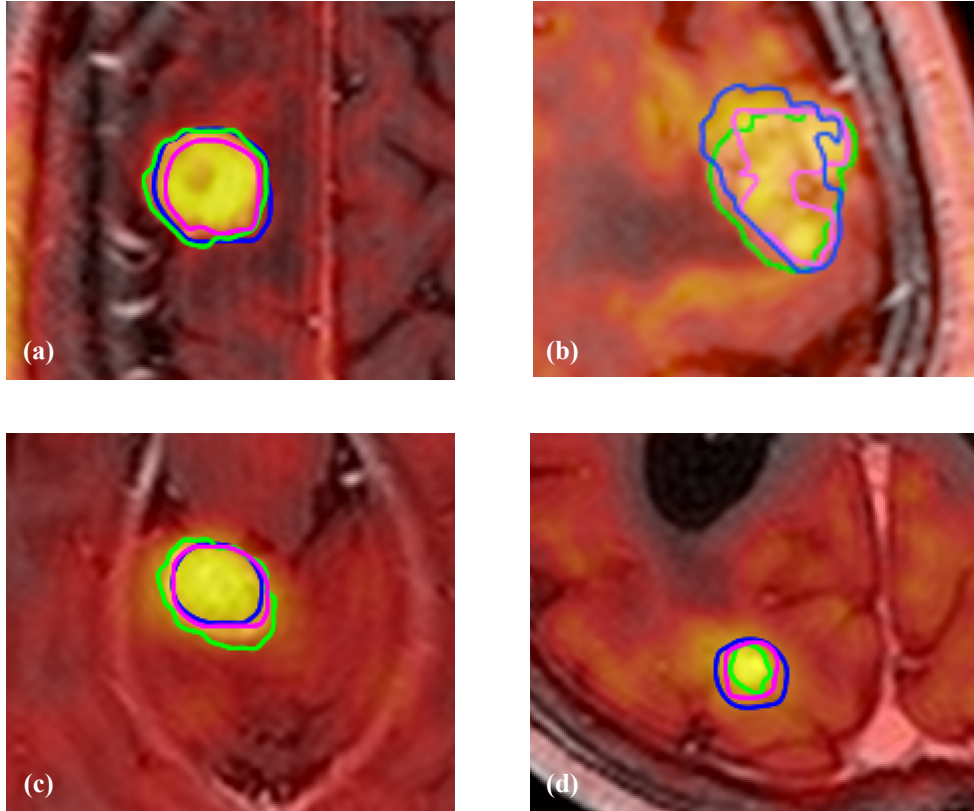
Figure 7 Graphical examples of co-segmentation results achieved by the proposed multimodal PET/MRI approach, where GTV (green contour), BTV (blue contour) and BTV$_{MRI}$ (magenta contour) ROIs are overlaid on the corresponding fused PET/MRI slices (displayed in Hot Look-Up Table). Four metastatic tumors in different anatomical regions of human brain are considered: **(a)** left temporo-parietal (tumor #3), **(b)** right temporo-parietal (tumor #11), **(c)** limbic (tumor #15), and **(d)** occipital (tumor #13) regions.

4.1. PET and MRI Tumor Volume Measurements

Volumes, calculated for each brain tumor imaged on MRI and PET modalities, are shown in Table 1. Absolute average volume difference (defined as $\text{abs}(V_1 - V_2)/V_2$) between BTV, BTV$_{MRI}$, and GTV were also calculated, in order to evaluate either overestimation or

41

underestimation of PET functional imaging with respect to anatomical MRI data, before and after GTV binary mask combination into PET images. In addition, Euclidean distances between BTV, BTV_{MRI}, and GTV centroids (centers of mass) were reported.

First of all, mean BTV and GTV values and their average absolute volume difference attest that tumor regions are imaged and represented differently on PET and MRI datasets. Furthermore, high standard deviation in BTV and GTV measurements proves that we are dealing with metastatic lesions characterized by various types and dimensions. On the other hand, BTV_{MRI} measurements follow a different trend because BTV_{MRI} segmentation is influenced by the combination of GTV masks and PET images, as proposed in section 3.2.4.4. Although we slightly integrate MRI ROIs with PET datasets during BTV_{MRI} computation, this conservative choice frequently could reduce radioactivity spill-in and spill-out effects, by exploiting higher MRI spatial resolution. This is evident in the examples shown in Figure 7. Moreover, BTV_{MRI} measurement standard deviation is lower than BTV and GTV ones. This means that multimodal PET/MRI segmentation yields more stable results with respect to single modality segmentations, since both metabolic and morphological imaging are considered. These experimental evidences are corroborated by the achieved absolute volume difference values, where BTV_{MRI} has about the same difference with GTV and BTV. Volume centroid distances reflect the aforementioned situation, too.

Table 1 Brain tumor volume measurement for each metastatic tumor using MR and PET imaging. Absolute volume difference and centroid distance between segmented GTV, BTV, and BTV$_{MRI}$ are also reported. Mean value (μ) and standard deviation (σ) are reported in the last two rows.

Tumor	GTV [voxels]	BTV [voxels]	BTV$_{MRI}$ [voxels]	Absolute volume difference [voxels]			Volume centroid distance [pixels]		
				BTV vs GTV	BTV$_{MRI}$ vs GTV	BTV vs BTV$_{MRI}$	BTV vs GTV	BTV$_{MRI}$ vs GTV	BTV vs BTV$_{MRI}$
#1	2267	3029	2380	33.61	4.98	27.27	1.805	1.067	1.457
#2	1546	1754	1297	13.45	16.11	35.24	1.523	0.740	0.839
#3	1945	1938	1561	0.36	19.74	24.15	1.250	0.949	0.398
#4	323	687	579	112.69	79.26	18.65	2.591	1.275	0.607
#5	346	484	417	39.88	20.52	16.07	1.446	0.845	0.246
#6	2293	2582	1996	12.60	12.95	29.36	0.974	0.971	0.098
#7	537	609	381	13.41	30.98	59.84	2.248	1.042	1.229
#8	1303	1010	1002	22.49	23.10	0.80	1.830	0.802	1.454
#9	286	122	159	57.34	44.41	23.27	2.238	1.681	0.399
#10	600	593	621	1.17	3.50	4.51	0.697	1.080	0.730
#11	2906	4052	2552	39.44	12.18	58.78	0.647	0.772	0.801
#12	210	226	138	7.62	34.29	63.77	3.118	2.720	0.447
#13	255	620	325	143.14	27.45	90.77	5.660	0.840	0.648
#14	2271	1202	1094	47.07	51.83	9.87	5.753	5.551	0.718
#15	1634	1129	1158	30.91	29.13	2.50	1.162	0.768	0.518
#16	2589	2491	1984	3.79	23.37	25.55	5.941	5.614	0.431
#17	1404	869	828	38.11	41.03	4.95	0.972	1.099	0.238
#18	2008	2398	1697	19.42	15.49	41.31	1.414	1.211	0.224
#19	7307	2238	1581	69.37	78.36	41.56	7.141	6.769	0.885
μ	1685.79	1475.42	1144.74	37.15	29.93	30.43	2.548	1.884	0.651
σ	1627.99	1081.92	749.63	37.59	21.37	24.22	2.018	1.890	0.395

The above observations, based on numerical experimental results, are qualitatively supported by the graphical multimodal PET/MRI segmentation results in Figure 8.

To measure the degree of dependence between GTV, BTV, and BTV$_{MRI}$, both Pearson's correlation coefficient ρ_P and Spearman's rank correlation coefficient ρ_S were calculated for each comparison.

Spearman's correlation yields different information with respect to Pearson's correlation, since Spearman's ρ_S is less sensitive to strong outliers that are in the tails of both samples. In fact, outlier importance is limited to the value of its rank.

As expected, GTV revealed greater correlation to BTV_{MRI}, especially according to Spearman's ρ_S. In addition, BTV and BTV_{MRI} are significantly correlated, using both Pearson and Spearman correlation coefficients. Accordingly, scatter diagrams in Figure 9 represent graphically these numerical results.
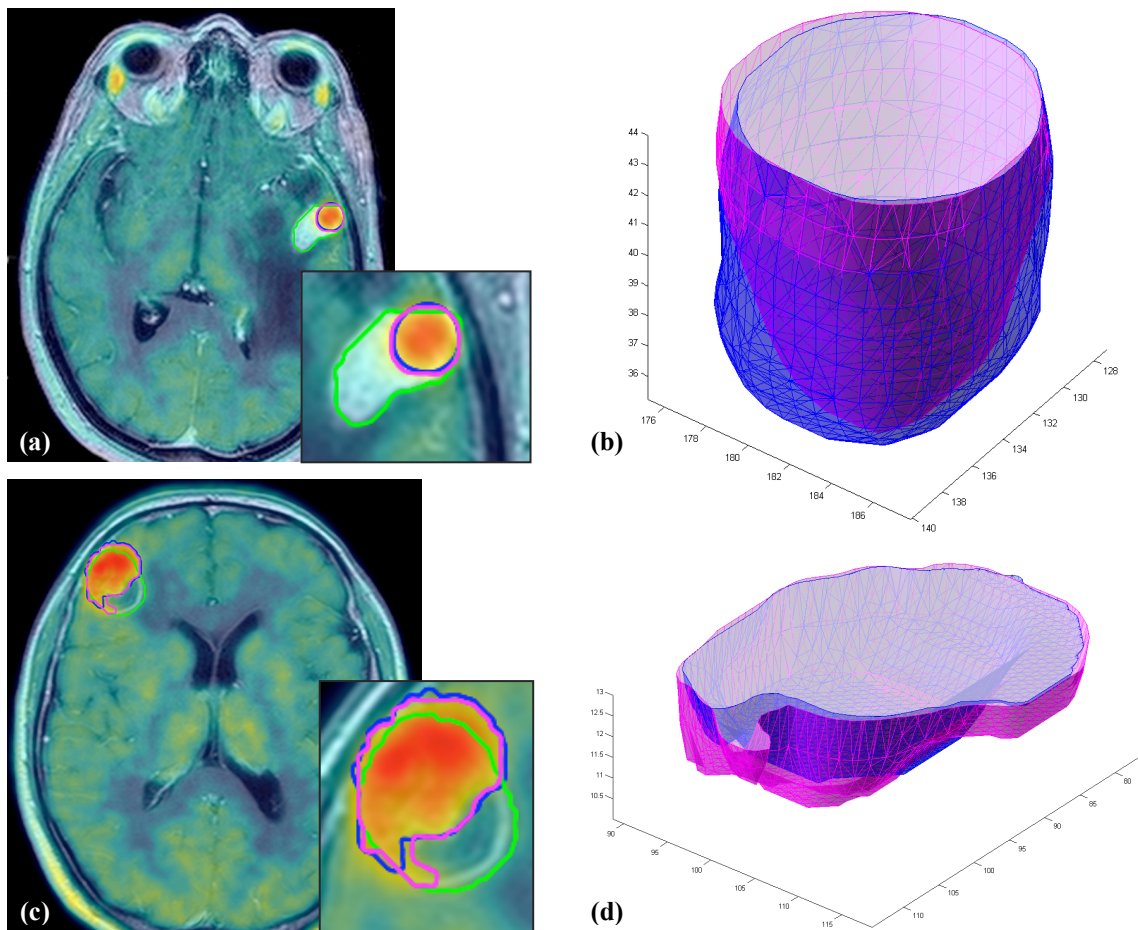
Figure 8 Segmentation results, on brain tumors #14 and #16, obtained by the single modality PET method (BTV) versus those obtained by the multimodal PET/MRI approach after the PET data updating based on the results of the MRI brain lesion segmentation (BTV_{MRI}): **(a, c)** GTV (green contour), BTV (blue contour), and BTV_{MRI} (magenta contour) ROIs overlaid on the corresponding fused PET/MRI slice (PET and MRI are displayed using Jet and grayscale LUTs, respectively); **(b, d)** 3D representation of BTV and BTV_{MRI} rendered with transparent surfaces (Alpha Blending with $\alpha = 0.40$), respectively, cut at the corresponding slice shown in (a) and (c).

44
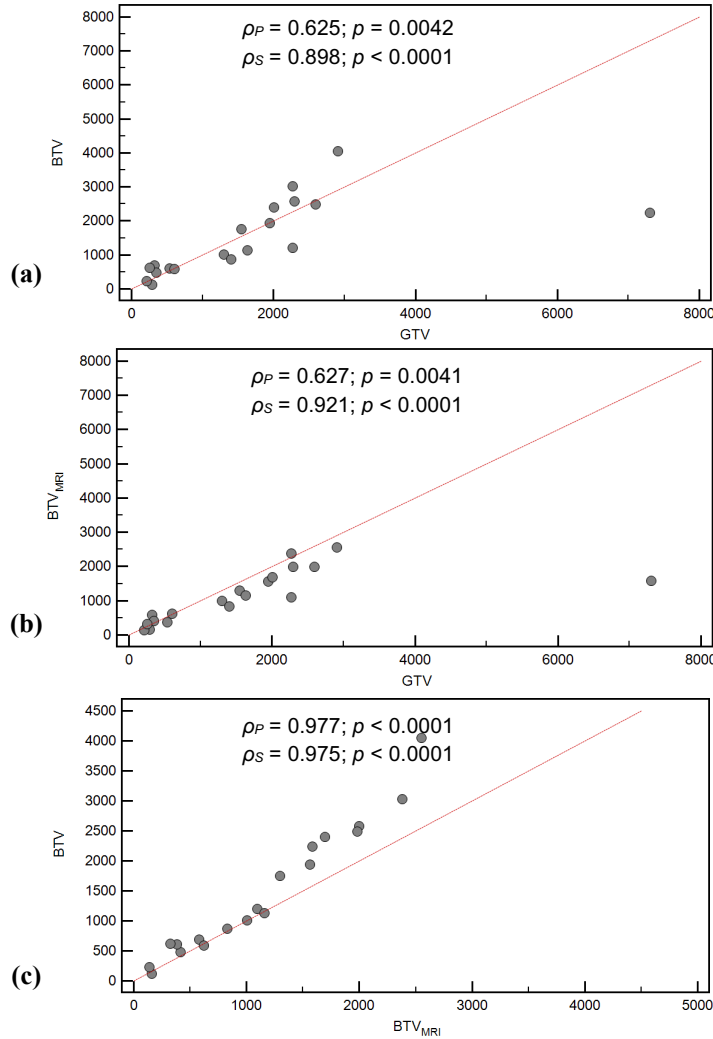
Figure 9 Scatter diagrams of tumor volume measurements: **(a)** BTV versus GTV; **(b)** BTV$_{MRI}$ versus GTV; **(c)** BTV versus BTV$_{MRI}$. Red dashed line is the line of equality. In the upper part of each sub-figure, Pearson and Spearman correlation coefficients with the corresponding significance level (*p* value) are also reported.

4.2. Evaluation of the Overall Multimodal PET/MRI Segmentation Method

In this section, an overall evaluation of the proposed multimodal PET/MRI segmentation method is presented. Spatial overlap-based, and distance-based metrics were calculated, to measure similarity and correlation concerning PET and MRI segmentation approaches, according to the theoretical description in sections 3.3.1 and 3.3.2.

Considering these results, it was possible to argue the complementarity between PET and MR imaging modalities, combined by the proposed multimodal segmentation method.

4.2.1. Tumor Spatial Overlap-based Metrics Results

Table 2 shows tumor spatial overlap-based metrics for PET and MRI segmentation methods. The achieved results demonstrated that GTV was, on average, more similar to BTV_{MRI} than to BTV. The highest mean values and the lowest standard deviation of the evaluation measures were obtained in BTV and BTV_{MRI} comparisons.

Table 2 Achieved tumor spatial overlap-based metrics for GTV, BTV, and BTV_{MRI} segmentations. Total average (μ) and standard deviation (σ) calculated on 19 brain lesions are also reported.

Tumor	Dice Similarity Coefficient [%]		
	BTV vs GTV	BTV_{MRI} vs GTV	BTV vs BTV_{MRI}
#1	63.97	78.89	76.17
#2	80.55	81.11	80.24
#3	81.33	79.81	83.91
#4	40.79	56.32	79.30
#5	55.42	59.24	73.70
#6	76.43	73.26	86.76
#7	58.29	78.46	62.22
#8	68.31	83.90	80.82
#9	39.22	51.24	83.99
#10	72.59	74.20	84.35
#11	65.74	78.71	68.14
#12	46.79	51.72	69.23
#13	52.57	76.90	68.36
#14	53.38	54.62	87.37
#15	76.66	79.08	89.81
#16	67.80	70.59	86.97
#17	65.55	67.03	85.80
#18	77.30	79.51	82.39
#19	32.85	31.66	78.24
μ	61.87	68.75	79.36
σ	14.64	14.07	7.79

4.2.2. Tumor Spatial Distance-based Metrics Results

Table 3 reports the values of spatial distance-based metrics achieved by the proposed multimodal PET/MRI segmentation approach in the experimental trials. Distance-based metrics values agreed with achieved volume-based and overlap-based measurements, showing the same trend.

Table 3 Achieved tumor spatial distance-based metrics for GTV, BTV, and BTV$_{MRI}$ segmentations. Total average (μ) and standard deviation (σ) calculated on 19 brain lesions are also reported.

Tumor	Hausdorff Distance [pixels]			Average Distance [pixels]			Mahalanobis Distance [pixels]		
	BTV vs GTV	BTV$_{MRI}$ vs GTV	BTV vs BTV$_{MRI}$	BTV vs GTV	BTV$_{MRI}$ vs GTV	BTV vs BTV$_{MRI}$	BTV vs GTV	BTV$_{MRI}$ vs GTV	BTV vs BTV$_{MRI}$
#1	8.544	6.403	7.616	2.669	1.377	1.756	0.412	0.264	0.339
#2	5.831	4.000	5.831	1.343	1.163	1.259	0.340	0.178	0.195
#3	8.485	7.810	4.472	1.400	1.355	1.145	0.436	0.312	0.138
#4	5.831	3.606	5.000	1.090	0.667	0.778	3.497	3.257	0.277
#5	5.385	3.000	3.606	1.295	0.798	0.742	1.857	1.814	0.107
#6	5.099	4.123	3.000	1.121	1.243	0.940	1.208	1.247	0.029
#7	9.220	4.000	5.831	2.233	0.804	1.332	0.786	0.441	0.421
#8	10.630	3.162	10.630	1.312	0.943	0.815	0.610	0.239	0.524
#9	4.472	4.472	1.414	0.727	0.969	0.204	1.392	0.994	0.377
#10	7.810	6.403	3.162	1.368	1.369	0.689	0.285	0.379	0.286
#11	12.000	6.083	11.662	2.630	1.535	2.262	0.734	0.180	0.214
#12	4.472	5.388	2.236	1.898	1.556	1.167	1.496	1.389	0.249
#13	7.280	2.828	7.280	2.345	0.809	1.711	0.530	0.404	0.296
#14	15.621	14.213	3.606	3.618	3.281	0.810	1.115	1.045	0.233
#15	4.243	3.606	2.236	1.250	1.107	0.643	0.286	0.219	0.147
#16	11.705	11.402	7.616	3.503	3.175	1.906	0.788	0.754	0.094
#17	5.385	4.243	2.236	2.136	1.939	0.769	0.267	0.319	0.087
#18	7.071	5.385	4.472	1.782	1.420	1.356	0.374	0.336	0.062
#19	15.811	16.125	10.000	5.820	5.811	1.486	1.446	1.360	0.195
μ	8.15	6.12	5.36	2.081	1.648	1.146	0.940	0.796	0.225
σ	3.57	3.79	3.04	1.211	1.235	0.515	0.787	0.778	0.131

4.2.3. Clinical Evaluation Results

Table 4 shows clinical evaluation results regarding both BTV and BTV$_{MRI}$ integration with GTV to determine CTV, according to the explanation in section 3.3.3.

In the current clinical practice the CTV is always based on the GTV (defined on MR images). As a consequence, the BTV contribution (defined on PET images) cannot get worse the CTV definition from a clinical perspective, i.e., the Likert score is always greater than 2.

Table 4 Clinical value of BTV and BTV$_{MRI}$, for each brain metastasis, in CTV definition[1].

Tumor	Clinical value	
	BTV integration	BTV$_{MRI}$ integration
#1	4	5
#2	4	4
#3	3	3
#4	4	4
#5	3	3
#6	4	5
#7	4	4
#8	3	3
#9	3	3
#10	3	3
#11	5	5
#12	3	3
#13	3	4
#14	4	4
#15	3	3
#16	4	4
#17	3	3
#18	4	5
#19	4	5

[1] Qualitative evaluation performed by three physicians using a five-point Likert scale, defined as: 1) strong worsening in CTV definition; 2) moderate worsening in CTV definition; 3) indifferent, neither enhancement nor worsening in CTV definition; 4) moderate enhancement in CTV definition; 5) strong enhancement in CTV definition.

In ~26% of cases, the CTV definition was strongly influenced by PET imaging. In more than 50% of cases, the CTV was strongly or moderately conditioned by metabolic imaging: only in 8/19 cases PET volume did not modify the CTV definition. In more than 25% of cases, BTV_{MRI} enhanced the CTV more accurately than BTV, because radioactivity spill-in and spill-out effects between tumor and surrounding tissues were reduced by the contribution of MRI ROIs in PET segmentation, shrinking false positive uptake areas.

5. Discussion

The proposed fully automated multimodal segmentation method introduces several novelties and advantages.

Firstly, we used two computer-assisted single modality segmentation approaches for PET and MR images, which have been already tested using evaluation metrics and validated by clinicians. Although image co-registration is needed to bring multimodal PET/MR image information into the same reference system, the co-segmentation results are not just derived via image registration since anatomical and metabolic are carefully integrated, by relying also on the physicians' expertise (see section 3.2.5), in the proposed multimodal PET/MRI segmentation algorithm. These accurate and operator-independent single modality segmentation methods are certainly more effective and reliable on PET and MRI datasets, with respect to approaches that unify information into a single graph.

State of the art methods based on a hyper-graph [21][42] or sub-graphs with inter-subgraph arcs [31] are more sensitive to registration errors, especially when multimodal images are not acquired contextually using a hybrid scanner. In these cases, no significant anatomical and functional changes have to be assumed between the images acquired with different modalities at the same clinical phase to directly construct the hyper-graph or the interconnected sub-graphs. The proposed approach was not tailored specifically for the latest generation hybrid PET/MRI scanners. Obviously, in the case of multimodal PET/MRI scanner, the scenario is simplified

considering that all the initial registration stages are not necessary, whereas the subsequent steps in the processing pipeline are still valid. Methods based on hyper-graphs generally yield a single target volume on the fused multimodal images. This may compromise the segmentation quality since PET and MRI could convey different information, resulting in a disagreement between BTV and GTV, because enhancement, edema, and necrosis regions are imaged differently by the PET and MRI modalities; so the tumor volumes defined on metabolic PET and on anatomic CT or MRI could be highly different [31]. The proposed multimodal method, keeping all anatomical and metabolic information and enabling a decision-level fusion [44], is more reliable on PET and MRI datasets with respect to approaches that unify information into a single graph structure. Result repeatability is ensured because it is able to adapt in different pathological scenarios. This choice allows for a greater awareness on the decision-making process, carried out by the clinical staff that is going to plan the neuro-radiosurgery treatment, that brings to the CTV definition. The CTV is determined by the clinical staff, by taking into account the specific patient's pathological scenario. According to the computed BTV and GTV volumes, the CTV identification is a deep decision-making process involving numerous anatomical and metabolic insights. Therefore, the appropriateness of the multimodal segmentation is justified by the addressed scenario, by allowing the clinicians to carefully consider the possibility to include BTV information into the planned CTV and to determine a personalized therapy for each single cancer metabolism [45].

Secondly, IURs detected on PET images (see section 3.2.4.1) are not blindly propagated to GTV segmentation algorithm, but properly modified according to MRI data using the developed ROI bounding region generation method, described in section 3.2.4.2. This *ad hoc* MRI-driven method, based on LSFs, finds adaptively a valid bounding region in order to eliminate user intervention, required by the MRI brain tumor segmentation method in [27] and [28]. On the other hand, in [42], the identified seeds on PET images are propagated to the corresponding anatomical images before segmentation process beginning. Hence, two existing and efficient

single modality processing pipelines are combined in a smart fashion. In particular, PET and MRI segmentation results are mutually exploited.

Lastly, this fully automated approach is very reproducible and reliable, also due to the brain anatomical district imaging. We focused on the application domain regarding brain tumors that underwent Leksell Gamma Knife stereotactic radiosurgery. In fact, the fully automatic identification of target IURs is feasible because MET-PET datasets for stereotactic neuro-radiosurgery treatment planning include only the brain area avoiding the possible presence of false positives in other anatomic regions. Differently, in total body FDG-PET examinations user interaction to manually identify the target lesion is always needed (normal structures such as brain, heart, bladder, kidneys, and ureters normally have high FDG uptake) [43]. Accordingly, these co-segmentation software implementation platforms must provide manual seeding facilities in addition to automated multimodal segmentation algorithm.

Although a one-to-one relationship between two different structural images of the same abnormal region could be reasonable, the assumption of identical lesion contours in both functional and morphologic images is often infeasible in many anatomical regions [42]. For instance, depending on the metabolic characteristics of the cells within a lung tumor [72], it may not take up a radiotracer in all its volume, or uptake region may be larger than the anatomical boundary of the tumor due to cellular activation in nearby tissues. Further issues are introduced by combining more than two structural modalities, i.e. MRI and CT, with PET metabolic imaging. Briefly, different imaging modalities (PET/MRI vs PET/CT), anatomic regions, and pathologies require a customization/adaptation of the method according to the specific clinical scenario.

In our study, PET and MRI datasets regarding the same subject were acquired at two different times (MRI is scanned a few days after MET-PET) by two different dedicated scanners. This represents a non trivial problem in co-segmentation domain, because an efficient and accurate multimodal co-registration is required. Instead, as explained in section 2, state of the art about

co-segmentation methods process mostly simultaneous PET/CT or PET/MRI acquisitions. Of course, the potential of hybrid imaging (PET/CT and PET/MRI systems) overcomes image registration issues by giving multimodal images contextually [73][74], especially in brain imaging [75].

The achieved experimental results showed that GTV and BTV segmentations are statistically correlated (Spearman's rank correlation coefficient: 0.898) but have not higher degree of similarity (average Dice Similarity Coefficient: 61.87 ± 14.64). In fact, GTV and BTV measurements as well as evaluation metrics values (volume-based, overlap-based, and spatial distance-based metrics) corroborated that MRI and MET-PET convey different but complementary imaging information. Furthermore, when lesion sizes are greater than 2-3 times the Full Width at Half Maximum (FWHM) of the point spread function of the PET image resolution reconstructed by the PET imaging system, the underestimation of metabolic activity due to PVE can be assumed to be negligible [76]. In other cases, a recovery coefficient method could be included in our algorithm, such as the approach described in [77]. Nevertheless, the output of the proposed multimodal PET/MRI segmentation method, named BTV_{MRI}, accurately combines PET and MR imaging. BTV_{MRI} segmentation could reduce radioactivity spill-in and spill-out effects between tumor and surrounding tissues, taking advantage of the higher spatial resolution of MRI.

In addition, since it is not possible to define a gold-standard CTV according to both MRI and PET images without treatment response assessment, the feasibility and the clinical value of BTV integration in Gamma Knife treatment planning were considered. Therefore, a visual and qualitative evaluation was performed by experienced physicians to assess the clinical value of BTV integration in CTV delineation using a five-point Likert scale. In most cases, CTV delineation was strongly or moderately influenced by PET imaging: GTV does not match with the functional area of the tumor, and metabolic imaging must be considered to assist the radiation oncologist in treatment planning. These results agree with [15], where in 74% the

expansion of the MET-PET volume was larger than the Gadolinium enhancement area. Table 4 shows that BTV_{MRI} influenced the CTV more accurately than BTV (in 5/19 of cases): this finding was attributed to the higher spatial resolution of MRI, which shrank small false positive areas in PET target segmentation (see section 3.2.4.4).

Finally, PET imaging should be usually considered by clinicians in order to determine a CTV that takes into account the "active" part of the cancer in addition to anatomical tumor boundaries. According to these findings, it is appropriate to include PET images in stereotactic neuro-radiosurgery treatment planning.

6. Conclusions

In this paper, a novel fully automatic multimodal segmentation method for Leksell Gamma Knife treatments was proposed. Two previously developed BTV [22][25][26] and GTV [27][28] segmentation methods on MET-PET and MR images, respectively, have been improved and combined in a smart fashion. The proposed multimodal PET/MRI segmentation approach yields a new BTV_{MRI}, which integrates PET and MR imaging.

To evaluate the effectiveness of our segmentation multimodal approach, experimental tests on 19 metastatic brain tumors were retrospectively performed. The proposed fully automatic multimodal PET/MRI segmentation approach is a valid operator-independent procedure to segment BTV and GTV. It has been proved that the BTV should be used to modify the GTV, considering both metabolic and morphologic information. By using our multimodal methodology, clinicians could be assisted in CTV delineation during stereotactic radiosurgery treatment planning. Therefore, the proposed multimodal segmentation approach can be considered clinically feasible, since it can be integrated in the current clinical practice.

After the positive opinion provided by clinicians, we have the rationale to begin clinical trials to evaluate tumor response after Leksell Gamma Knife treatment execution, even when BTV is included in CTV delineation during planning phase.

Conflict of Interest Statement

All authors in this paper have no potential conflict of interest.

Acknowledgments

References

[1]   L. Leksell, Stereotactic radiosurgery, J. Neurol. Neurosurg. Psychiatry 46 (1983) 797-803. doi: 10.1136/jnnp.46.9.797.

[2]   G. Luxton, Z. Petrovich, G. Jozsef, L.A. Nedzi, M.L. Apuzzo, Stereotactic radiosurgery: principles and comparison of treatment methods, Neurosurgery 32 (2) (1993) 241-259. doi: 10.1227/00006123-199302000-00014.

[3]   M.Y. Law and B. Liu, DICOM-RT and its utilization in radiation therapy, Radiographics 29 (3) (2009) 655-667. doi: 10.1148/rg.293075172.

[4]   B.N. Joe, M.B. Fukui, C.C. Meltzer, Q.S. Huang, R.S. Day, P.J. Greer, M.E. Bozik, Brain tumor volume measurement: comparison of manual and semiautomated methods, Radiology 212 (3) (1999) 811-816. doi: 10.1148/radiology.212.3.r99se22811.

[5]   V.S. Khoo and D.L. Joon, New developments in MRI for target volume delineation in radiotherapy, Br. J. Radiol. 79 Special Issue 1 (2006) S2-S15. doi: 10.1259/bjr/41321492.

[6]   A.W. Beavis, P. Gibbs, R.A. Dealey, V.J. Whitton, Radiotherapy treatment planning of brain tumours using MRI alone, Br. J. Radiol. 71 (845) (1998) 544-548. doi: 10.1259/bjr.71.845.9691900.

[7]   G.H. Bol, A.N.T.J. Kotte, U.A. van der Heide, J.J.W. Lagendijk, Simultaneous multi-modality ROI delineation in clinical practice, Comput. Methods Programs Biomed. 96 (2) (2009) 133-140. doi: 10.1016/j.cmpb.2009.04.008.

[8]   P.M. Evans, Anatomical imaging for radiotherapy, Phys. Med. Biol. 53 (12) (2008) R151-R191. doi: 10.1088/0031-9155/53/12/R01.

[9]   V. Moskvin, C. DesRosiers, L. Papiez, R. Timmerman, M. Randall, P. DesRosiers, Monte Carlo simulation of the Leksell Gamma Knife®: I. Source modelling and calculations in homogeneous media. Phys. Med. Biol. 47 (12) (2002) 1995-2001. doi: 10.1088/0031-9155/47/12/301.

[10]   A. Wu, Physics and dosimetry of the gamma knife, Neurosurg. Clin. N. Am. 3 (1) (1992) 35-50. PMID: 1633451.

[11]   Q.J. Wu and J.D. Bourland, Morphology-guided radiosurgery treatment planning and optimization for multiple isocenters, Med. Phys. 26 (10) (1999) 2151-2160. doi: 10.1118/1.598731.

[12]   R.L. Wahl, H. Jacene, Y. Kasamon, M.A. Lodge, From RECIST to PERCIST: evolving considerations for PET response criteria in solid tumors, J. Nucl. Med. 50 (2009) 122S-150S. doi: 10.2967/jnumed.108.057307.

[13]   M. Levivier, D. Wikier, S. Goldman, P. David, T. Metens, N. Massager, et al., Integration of the metabolic data of positron emission tomography in the dosimetry planning of radiosurgery with the Leksell gamma knife: early experience with brain tumors, J. Neurosurg. 93 (Supplement 3) (2000) 233-238. doi: 10.3171/jns.2000.93.supplement 3.0233.

[14]   K. Miwa, M. Matsuo, J. Shinoda, T. Aki, S. Yonezawa, T. Ito, Y. Asano, M. Yamada, K. Yokoyama, J. Yamada, H. Yano, T. Iwama, Clinical value of [11C]methionine PET for stereotactic radiation therapy with intensity modulated radiation therapy to metastatic brain tumors, Int. J. Radiat. Oncol. Biol. Phys. 84 (5) (2012) 1139-1144. doi:10.1016/j.ijrobp.2012.02.032.

[15]   A.L. Grosu, W.A. Weber, E. Riedel, B. Jeremic, C. Nieder, M. Franz, H. Gumprecht, R. Jaeger, M. Schwaiger, M. Molls, L-(methyl-11C) methionine positron emission tomography for target delineation in resected high-grade gliomas before radiotherapy, Int. J. Radiat. Oncol. Biol. Phys. 63 (1) (2005) 64-74. doi: 10.1016/j.ijrobp.2005.01.045.

[16]   P. Heiss, S. Mayer, M. Herz, H.J. Wester, Investigation of transport mechanism and uptake kinetics of O-(2-[18F]fluoroethyl)-Ltyrosine in vitro and in vivo, J. Nucl. Med. 40 (1999) 1367-1373. PMID: 10450690.

[17]   A.L. Grosu, W. Weber, M. Franz, S. Stärk, M. Piert, R. Thamm, H. Gumprecht, M. Schwaiger, M. Molls, C. Nieder, Reirradiation of recurrent high-grade gliomas using amino acid PET (SPECT)/CT/MRI image fusion to determine gross tumor volume for stereotactic fractionated radiotherapy, Int. J. Radiat. Oncol. Biol. Phys. 63 (2) (2005) 511-519. doi: 10.1016/j.ijrobp.2005.01.056.

[18]   M.W. Gross, W.A. Weber, H.J. Feldmann, P.B., M. Schwaiger, M. Molls, The value of F-18-fluorodeoxyglucose PET for the 3-D radiation treatment planning of malignant gliomas, Int. J. Radiat. Oncol. Biol. Phys. 41 (5) (1998) 989-995. doi: 10.1016/S0360-3016(98)00183-7.

[19]   D. Delbeke, Oncological applications of FDG PET imaging: brain tumors, colorectal cancer lymphoma and melanoma, J. Nucl. Med. 40 (4) (1999) 591-603. PMID: 10210218.

[20]   A.L. Grosu and W.A. Weber, PET for radiation treatment planning of brain tumours, Radiother. Oncol. 96 (3) (2010) 325-327. doi:10.1016/j.radonc.2010.08.001.

[21]   D. Han, J. Bayouth, Q. Song, A. Taurani, M. Sonka, J. Buatti, X. Wu, Globally optimal tumor segmentation in PET-CT images: a graph-based co-segmentation method, in: Proceeding of the 22nd International Conference on Information Processing in Medical Imaging, IPMI 2011, Kloster Irsee, Germany, 3-8 July 2011, pp. 245-256, Lecture Notes in Computer Science 6801 (Springer Berlin Heidelberg, 2011). doi: 10.1007/978-3-642-22092-0_21.

[22]   A. Stefano, S. Vitabile, G. Russo, M. Ippolito, F. Marletta, C. D'Arrigo, D. D'Urso, M.G. Sabini, O. Gambino, R. Pirrone, E. Ardizzone, M.C. Gilardi, An automatic method for metabolic evaluation of gamma knife treatments, in: Proceedings of the 18th International Conference Image Analysis and Processing, ICIAP, Genoa, Italy, 7-11 September 2015, Part I, pp. 579-589, Lecture Notes in Computer Science 9279 (Springer International Publishing, 2015). doi: 10.1007/978-3-319-23231-7_52.

[23]   P. Georgiadis, D. Cavouras, I. Kalatzis, A. Daskalakis, G.C. Kagadis, K. Sifaki, M. Malamas, G. Nikiforidis, E. Solomou, Improving brain tumor characterization on MRI by probabilistic neural networks and non-linear transformation of textural features, Comput. Methods Programs Biomed. 89 (1) 2008 24-32. doi: 10.1016/j.cmpb.2007.10.007.

[24]   Z. Xu, U. Bagci, J.K. Udupa, J. K., D.J. Mollura, Fuzzy connectedness image co-segmentation for hybrid PET/MRI and PET/CT scans, in: Computational Methods for Molecular Imaging, Part I, pp. 15-24, Lecture Notes in Computational Vision and Biomechanics 22 (Springer International Publishing, 2015). doi: 10.1007/978-3-319-18431-9_2.

[25]   A. Stefano, S. Vitabile, G. Russo, M. Ippolito, D. Sardina, M.G. Sabini, F. Gallivanone, I. Castiglioni, M.C. Gilardi, A graph-based method for PET image segmentation in radiotherapy planning: A pilot study, in: A. Petrosino (Ed.), Proceedings of the 17th International Conference on Image Analysis and Processing, ICIAP, Naples, Italy, 9-13 September 2013, Part II, pp. 711-720, Lecture Notes in Computer Science 8157 (Springer Berlin Heidelberg, 2013). doi: 10.1007/978-3-642-41184-7_72.

[26]   A. Stefano, S. Vitabile, G. Russo, M. Ippolito, F. Marletta, C. D'Arrigo, D. D'Urso, M. Sabini, O. Gambino, R. Pirrone, E. Ardizzone, M. Gilardi, A Fully Automatic Method for Biological Target Volume Segmentation of Brain Metastases, Int. J. Imaging Syst. Technol. 26 (1) (2016) 29–37. doi: 10.1002/ima.22154.

[27]   L. Rundo, C. Militello, S. Vitabile, G. Russo, P. Pisciotta, F. Marletta, M. Ippolito, C. D'Arrigo, M. Midiri, M.C. Gilardi, Semi-automatic brain lesion segmentation in gamma knife treatments using an unsupervised fuzzy C-means clustering technique, In: Advances in Neural Networks: Computational Intelligence for ICT,

Smart Innovation, Systems and Technologies, Vol. 54, pp. 15-26 (Springer International Publishing, 2016). doi: 10.1007/978-3-319-33747-0_2.

[28]   C. Militello, L. Rundo, S. Vitabile, G. Russo, P. Pisciotta, F. Marletta, M. Ippolito, C. D'Arrigo, M. Midiri, M.C. Gilardi, Gamma Knife treatment planning: MR brain tumor segmentation and volume measurement based on unsupervised fuzzy C-means clustering, Int. J. Imaging Syst. Technol. 25 (3) (2015) 213-225. doi:10.1002/ima.22139.

[29]   L. Grady, Random walks for image segmentation, IEEE Trans. Pattern Anal. Mach. Intell. 28 (11) (2006) 1768-1783. doi: 10.1109/TPAMI.2006.233.

[30]   J.C. Bezdek, R. Ehrlich, W. Full, FCM: the fuzzy C-means clustering algorithm, Comput. Geosci. 10 (2) (1984) 191-203. doi: 10.1016/0098-3004(84)90020-7.

[31]   Q. Song, J. Bai, D. Han, S. Bhatia, W. Sun, W. Rockey, J.E. Bayouth, J.M. Buatti, Optimal co-segmentation of tumor in PET-CT images with context information, IEEE Trans. Med. Imaging 32 (9) (2013) 1685-1697. doi: 10.1109/TMI.2013.2263388.

[32]   H. Yu, C. Caldwell, K. Mah, D. Mozeg, Coregistered FDG PET/CT-Based textural characterization of head and neck cancer for radiation treatment planning, IEEE Trans. Med. Imaging 28 (3) (2009) 374-383. doi: 10.1109/TMI.2008.2004425.

[33]   Y. Xia, L. Wen, S. Eberl, M. Fulham, D. Feng, Segmentation of dual modality brain PET/CT images using the MAP-MRF model, in: Proceedings of the 10th IEEE Workshop on Multimedia Signal Processing, 8-10 Oct. 2008, pp.107-110. doi: 10.1109/MMSP.2008.4665057.

[34]   Y. Xia, S. Eberl, L. Wen, M. Fulham, D.D. Feng, Dual-modality brain PET-CT image segmentation based on adaptive use of functional and anatomical information, Comput. Med. Imaging Graph. 36 (1) (2012) 47-53. doi: 10.1016/j.compmedimag.2011.06.004.

[35]   V. Potesil, X. Huang, X.S. Zhou, Automated tumor delineation using joint PET/CT information, in: M.L. Giger and N. Karssemeijer (Eds.), Medical Imaging 2007: Computer-Aided Diagnosis, Proceedings of the SPIE 6514, 2007, pp. 65142Y-65142Y-8. doi:10.1117/12.710216.

[36]   M. Vallières, C.R. Freeman, S.R., Skamene, I. El Naqa, A radiomics model from joint FDG-PET and MRI texture features for the prediction of lung metastases in soft-tissue sarcomas of the extremities, Phys. Med. Biol. 60 (14) (2015) 5471. doi:10.1088/0031-9155/60/14/5471.

[37]   A. Yezzi, L. Zollei, T. Kapur, A variational framework for joint segmentation and registration, in: Proceedings of the IEEE Workshop on Mathematical Methods in Biomedical Image Analysis 2001, MMBIA 2001, pp.44-51. doi: 10.1109/MMBIA.2001.991698.

[38]   J. Wojak, E.D. Angelini, E.D, I. Bloch, Joint variational segmentation of CT-PET data for tumoral lesions, in: Proceedings of the 2010 IEEE International Symposium on Biomedical Imaging: From Nano to Macro, 14-17 April 2010, pp. 217-220. doi: 10.1109/ISBI.2010.5490374.

[39]   I. El Naqa, D. Yang, A. Apte, D. Khullar, S. Mutic, J. Zheng, J.D. Bradley, P. Grigsby, J.O. Deasy, Concurrent multimodality image segmentation by active contours for radiotherapy treatment planning, Med. Phys. 34 (12) (2007) 4738-4749. doi: 10.1118/1.2799886.

[40]   S. Leibfarth, F. Eckert, S. Welz, C. Siegel, H. Schmidt, N. Schwenzer, D. Zips, D. Thorwarth, Automatic delineation of tumor volumes by co-segmentation of combined PET/MR data, Phys. Med. Biol. 60 (14) (2015) 5399-5412. doi: 10.1088/0031-9155/60/14/5399.

[41]   U. Bagci, G. Kramer-Marek, D.J. Mollura, Automated computer quantification of breast cancer in small-animal models using PET-guided MR image co-segmentation, EJNMMI Res. 3 (1:49) 1-13 (Springer Berlin Heidelberg, 2013). doi: 10.1186/2191-219X-3-49.

[42]   U. Bagci, J.K. Udupa, N. Mendhiratta, B. Foster, Z. Xu, J. Yao, X. Chen, D.J. Mollura, Joint segmentation of anatomical and functional images: applications in quantification of lesions from PET, PET-CT, MRI-PET, and MRI-PET-CT images, Med. Image Anal. 17 (8) (2013) 929-945. doi: 10.1016/j.media.2013.05.004.

[43]   A. Stefano, S. Vitabile, G. Russo, M. Ippolito, M.G. Sabini, D. Sardina, O. Gambino, R. Pirrone, E. Ardizzone, M.C. Gilardi, An enhanced random walk algorithm for delineation of head and neck cancers in PET studies, Med. Biol. Eng. Comput. (2016) 1-12, first online: 16 September 2016. doi: 10.1007/s11517-016-1571-0.

[44]   V. Conti, C. Militello, F. Sorbello, S. Vitabile, A frequency-based approach for features fusion in fingerprint and iris multimodal biometric identification systems, IEEE Trans. Syst. Man. Cybern. Part C 40 (4) (2010) 384-395. doi: 10.1109/TSMCC.2010.2045374.

[45]   M. Brady, R. Highnam, B. Irving, J.A. Schnabel, Oncological image analysis, Med. Image Anal. 33 (2016) 7-12. doi: 10.1016/j.media.2016.06.012.

[46]   F. Schoonjans, A. Zalata, C.E. Depuydt, F.H. Comhaire, MedCalc: a new computer program for medical statistics, Comput. Methods Programs Biomed. 48 (3) (1995) 257-262. doi: 10.1016/0169-2607(95)01703-8.

[47]   C. Militello, S. Vitabile, L. Rundo, G. Russo, M. Midiri, M.C. Gilardi, A Fully Automatic 2D Segmentation Method for Uterine Fibroid in MRgFUS Treatment Evaluation, Comput. Biol. and Med. (62) (2015) 277-292. doi: 10.1016/j.compbiomed.2015.04.030.

[48]   N.R. Pal, J.C. Bezdek, On cluster validity for the fuzzy C-means model. IEEE Trans. Fuzzy Syst. 3 (3) (1995) 370-379. doi: 10.1109/91.413225.

[49]   R.D. Ambrosini, P. Wang, W.G. O'Dell, Computer-aided detection of metastatic brain tumors using automated three-dimensional template matching, J. Magn. Reson. Imaging, 31 (1) (2010) 85-93. doi: 10.1002/jmri.22009.

[50]   W. Dou, S.Ruan, Y. Chen, D.Bloyet, J.M. Constans, A framework of fuzzy information fusion for the segmentation of brain tumor tissues on MR images, Image Vis. Comput. 25 (2) (2007) 164-171. doi: 10.1016/j.imavis.2006.01.025.

[51]   R. Shah, S, Vattoth, R. Jacob, F.F.P. Manzil, J.P. O'Malley, P. Borghei, B.N. Patel, J.K. Curé, Radiation necrosis in the brain: imaging features and differentiation from tumor recurrence, Radiographics 32 (5) (2012)1343-1359. doi: 10.1148/rg.325125002.

[52]   F. Maes, A. Collignon, D. Vandermeulen, G. Marchal, P. Suetens, P., Multimodality image registration by maximization of mutual information, IEEE Trans. Med. Imaging 16 (2) (1997) 187-198. doi: 10.1109/42.563664.

[53]   J.P.W. Pluim, J.B.A. Maintz, M.A. Viergever, Mutual-information-based registration of medical images: a survey, IEEE Trans. Med. Imaging 22 (8) (2003) 986-1004. doi: 10.1109/TMI.2003.815867.

[54]   W.D. Penny, K.J. Friston, J.T. Ashburner, S.J. Kiebel, T.E. Nichols, Statistical parametric mapping: the analysis of functional brain images, First Edition (Academic Press, 2011). ISBN: 9780123725608.

[55]   A. Collignon, F. Maes, D. Delaere, D. Vandermeulen, P. Suetens, G. Marchal, Automated multi-modality image registration based on information theory, in: Y. Bizais, C. Barillot, and R. Di Paola (Eds.), Proceedings of Information Processing in Medical Imaging, IPMI 1995, pp. 263-274 (Kluwer Academic Publishers, Dordrecht, The Netherlands, 1995).

[56]   J. Čížek, K. Herholz, S. Vollmar, R. Schrader, J. Klein, W.D. Heiss, Fast and robust registration of PET and MR images of human brain, NeuroImage 22 (1) (2004) 434-442. doi: 10.1016/j.neuroimage.2004.01.016.

[57]   J.P.W. Pluim, J.B.A. Maintz, M.A. Viergever, Image registration by maximization of combined mutual information and gradient information, IEEE Trans. Med. Imaging 19 (8) (2000) 809-814. doi: 10.1109/42.876307.

[58]   C. Studholme, D.L.G. Hill, D.J. Hawkes, An overlap invariant entropy measure of 3D medical image alignment, Pattern Recognit. 32 (1) (1999) 71-86. doi: 10.1016/S0031-3203(98)00091-0.

[59]   P. Thevenaz, T. Blu, M. Unser, Interpolation revisited [medical images application], IEEE Trans. Med. Imaging 19 (7) (2000) 739-758. doi: 10.1109/42.875199.

[60]   E.J. Breen, R. Jones, H. Talbot, Mathematical morphology: a useful set of tools for image analysis, Stat. Comput. 10 (2) (2000) 105-120. doi: 10.1023/A:1008990208911.

[61] C. Li, C. Xu, C., Gui, M.D. Fox, Distance regularized level set evolution and its application to image segmentation, IEEE Trans. Image Process. 19 (12) (2000) 3243-3254. doi: 10.1109/TIP.2010.2069690.

[62] L. Rundo, C. Militello, S. Vitabile, C. Casarino, G. Russo, M. Midiri, M.C. Gilardi, Combining Split-and-Merge and Multi-Seed Region Growing Algorithms for Uterine Fibroid Segmentation in MRgFUS Treatments, Med. Biol. Eng. Comput., 54 (7) (2016) 1071-1084. doi: 10.1007/s11517-015-1404-6.

[63] S. Osher, J.A. Sethian, Fronts propagating with curvature-dependent speed: algorithms based on Hamilton-Jacobi formulations, J. Comput. Phys. 79 (1) (1988) 12-49. doi: 10.1016/0021-9991(88)90002-2.

[64] H.K. Zhao, T. Chan, B. Merriman, S. Osher, A variational level set approach to multiphase motion, J. Comput. Phys. 127 (1) (1996) 179-195. doi: 10.1006/jcph.1996.0167.

[65] V.G. Kanas, E.I. Zacharaki, C. Davatzikos, K.N. Sgarbas, V. Megalooikonomou, A low cost approach for brain tumor segmentation based on intensity modeling and 3D Random Walker, Biomed. Signal Process. Control 22 (2015) 19-30. doi: 10.1016/j.bspc.2015.06.004.

[66] H.C. Huang, Y.Y. Chuang, C.S. Chen, Multiple Kernel Fuzzy Clustering, IEEE Trans. Fuzzy Syst. 20 (1) (2012) 120-134. doi: 10.1109/TFUZZ.2011.2170175.

[67] A. Stefano, F. Gallivanone, C. Messa, M.C., Gilardi, I. Castiglioni, Metabolic impact of partial volume correction of [18F] FDG PET-CT oncological studies on the assessment of tumor response to treatment, Q. J. Nucl. Med. Mol. Imaging 58 (4) (2014) 413-423. ISSN: 1824-4785. PMID: 24732680.

[68] A.A. Taha and A. Hanbury, Metrics for evaluating 3D medical image segmentation: analysis, selection, and tool, BMC Med. Imaging 15 (1) (2015) 1-28. doi: 10.1186/s12880-015-0068-x.

[69] A. Fenster and B. Chiu, Evaluation of segmentation algorithms for medical imaging, in: Proceedings of the 27th Annual International Conference of the IEEE Engineering in Medicine and Biology Society, IEEE-EMBS 2005, pp. 7186-7189. doi: 10.1109/IEMBS.2005.1616166.

[70] Y.J. Zhang, A review of recent evaluation methods for image segmentation, in: Proceedings of the Sixth IEEE International Symposium on Signal Processing and its Applications, ISSPA 2001, Vol. 1, pp. 148-151. doi: 10.1109/ISSPA.2001.949797.

[71] R. Cárdenes, R. de Luis-García, M. Bach-Cuadra, A multidimensional segmentation evaluation for medical image data, Comput. Methods Programs Biomed. 96 (2) (2009) 108-124. doi: 10.1016/j.cmpb.2009.04.009.

[72] C. Ballangan, X. Wang, M. Fulham, S. Eberl, D.D. Feng, Lung tumor segmentation in PET images using graph cuts, Comput. Methods Programs Biomed. 109 (3) (2013) 260-268. doi: 10.1016/j.cmpb.2012.10.009.

[73] B.J. Pichler, M.S. Judenhofer, C. Pfannenberg, Multimodal imaging approaches: PET/CT and PET/MRI, in: Mol. Imaging I, pp. 109-132 (Springer Berlin Heidelberg, 2008). doi: 10.1007/978-3-540-72718-7_6.

[74]   B. Weissler, P. Gebhardt, P.M. Dueppenbecker, J. Wehner, D. Schug, C.W. Lerche, B. Goldschmidt, A. Salomon, I. Verel, E. Heijman, M. Perkuhn, D. Heberling, R.M. Botnar, F. Kiessling, V. Schulz, A digital preclinical PET/MRI insert and initial results, IEEE Trans. Med. Imaging 34 (11) (2015) 2258-2270. doi: 10.1109/TMI.2015.2427993.

[75]   W.D. Heiss, The potential of PET/MR for brain imaging. Eur. J. Nucl. Med. Mol. Imaging 36 (Supplement 1) (2009) 105-112. doi: 10.1007/s00259-008-0962-3.

[76]   V.M. Soret, S.L. Bacharach, I. Buvat, Partial-volume effect in PET tumor imaging, J. Nucl. Med. 48 (6) (2007) 932-945. doi: 10.2967/jnumed.106.035774

[77]   F. Gallivanone, A. Stefano, E. Grosso, C. Canevari, L. Gianolli, C. Messa, M.C. Gilardi, I. Castiglioni, PVE correction in PET-CT whole-body oncological studies from PVE-affected images, IEEE Trans. Nucl. Sci. 58 (3) (2011) 736-747. doi: 10.1109/TNS.2011.2108316.